



## The role of circular folds in mixing intensification in the small intestine: A numerical study

Jinping Zha <sup>a</sup>, Siyu Zou <sup>a</sup>, Jianyu Hao <sup>b</sup>, Xinjuan Liu <sup>b</sup>, Guillaume Delaplace <sup>c</sup>, Romain Jeantet <sup>d</sup>, Didier Dupont <sup>d</sup>, Peng Wu <sup>a</sup>, Xiao Dong Chen <sup>a</sup>, Jie Xiao <sup>a,\*</sup>

<sup>a</sup> School of Chemical and Environmental Engineering, College of Chemistry, Chemical Engineering and Materials Science, Soochow University, Suzhou, Jiangsu Province 215123, China

<sup>b</sup> Department of Gastroenterology, Beijing Chaoyang Hospital, Capital Medical University, Chaoyang District, Beijing 100024, China

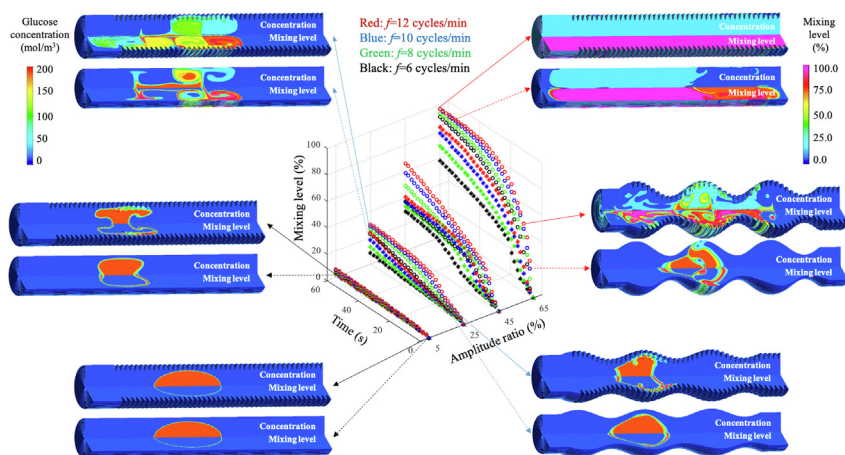
<sup>c</sup> UMET – Unité Matériaux et Transformations, UMR 8207 (Univ. Lille, CNRS, INRAE, Centrale Lille), 59000 Lille, France

<sup>d</sup> STLO, INRAE, Institut Agro, 35042 Rennes, France

### HIGHLIGHTS

- Numerical simulation of mixing in a human duodenum featuring circular folds.
- Tracking evolving concentration and mixing level distributions under segmentation.
- Mixing intensification by prominent vortices with high velocity and shear rate.
- Promoting mixing by tall and slim folds with enlarged segmentation amplitude, frequency and wavelength.

### GRAPHICAL ABSTRACT



### ARTICLE INFO

#### Article history:

Received 30 April 2020

Received in revised form 2 August 2020

Accepted 23 August 2020

Available online 29 August 2020

#### Keywords:

Small intestine  
Circular folds/Plicae circulares  
Segmentation  
Mixing  
Process intensification  
Soft elastic reactor (SER)

### ABSTRACT

The inner wall of the intestine has multiscale structures whose roles, beyond the increase of surface area for absorption, are yet to be discovered. In this study, the mixing process in a human duodenum with circular folds, driven by segmentation contraction, was simulated using a multiphysics model, making it possible to track the evolution of mixing level distributions and enabling quantitative evaluation of the structural role of folds in mixing intensification. It was found that, in a laminar flow regime, circular folds intensify both radial and axial mixing by synergistically offering prominent and long-lasting swirls/vortices, high fluid velocity and high shear rates. Tall and slim folds with enlarged segmentation amplitude, frequency and wavelength can enhance mixing. The maximum enhancement ratio can reach 6.18 under the investigated conditions. These findings will also be valuable for the improved design of biomimetic soft-elastic reactors for the chemical and pharmaceutical industries.

© 2020 Elsevier Ltd. All rights reserved.

\* Corresponding author.

E-mail address: jie.xiao@suda.edu.cn (J. Xiao).

## Nomenclature

### Symbols

$a$	Distance from pylorus to the 1st fold (m)
$b$	The contraction starts away from the pylorus (m)
$c$	Concentration ( $\text{mol}/\text{m}^3$ )
$c_0$	Initial concentration ( $\text{mol}/\text{m}^3$ )
$D$	Diffusion coefficient ( $\text{m}^2/\text{s}$ )
$f$	Frequency (cycles/min)
$h_f$	Height of circular folds (m)
$I$	Unit tensor (-)
$L$	Length of the duodenum (m)
$M$	Molecular weight (g/mol)
$n$	The index of the circular folds (-)
$p$	Fluid pressure (Pa)
$P$	Function of position (m)
$r, z, \theta$	Cylindrical coordinates (m, m, °)
$r^I, r^{II}$	$r$ -direction position of lumen wall of Systems 1 and 2, respectively (m)
$r_f$	Radius of circular folds (m)
$R$	Radius (m)
$R_0$	Radius of System 1 (m)
$R'_0$	Radius of System 2 (m)
$t$	Time (s)
$T$	Cycle (s)
$u$	Fluid velocity ( $\text{m}/\text{s}$ )
$V$	Volume ( $\text{m}^3$ )
$v_g$	Volume ratio of glucose (-)
$w_f$	Width of circular folds (m)
$Y$	Mass fraction (-)

$2z_0$  Distance between two adjacent folds (m)

### Greek letters

$\alpha$	Enhancement ratio (-)
$\Gamma$	Function of time (-)
$\delta$	Depth (m)
$\varepsilon^*$	Ratio of amplitude to radius (%)
$\lambda$	Wavelength (m)
$\mu$	Fluid viscosity ( $\text{Pa}\cdot\text{s}$ )
$\xi$	Ratio of height to width of a fold (-)
$\rho$	Density ( $\text{kg}/\text{m}^3$ )
$\chi$	Mixing level (%)
$\omega$	Distribution density of circular folds (folds/m)

### Superscripts

$I$	System 1 (with folds)
$II$	System 2 (without folds)

### Subscripts

$c$	Characteristic
$f$	Circular folds
$g$	Glucose
$i$	Index of species
$j$	Index of mesh element
$m$	Mixture
$w$	Water
$\infty$	The ideally mixed state

## 1. Introduction

Food provides the body with essential nutrients and energy so that normal human physiological activities can be maintained. Efficient digestion and absorption processes are critical for human health. After being ingested, food is further digested by the stomach and then enters the small intestine where the chyme is mixed and reacts with intestinal fluids that include enzymes, bile and pancreatic juices. Carbohydrates, proteins and fats are converted into absorbable nutrient molecules in the intestine. Driven by intestinal motility, the nutrients are then transferred to the wall of the intestine and eventually absorbed (Hall, 2016; Marieb and Keller, 2018).

It should be noted that both digestion and absorption in humans essentially take place in the small intestine. The small intestine has been a focus of research for many years because of its importance in the digestive process (Bayliss and Starling, 1899). However, our understanding of the digestion and absorption process in this organ is far from complete due to the high complexity of the system. In addition to complex motility, the structure of the intestinal wall demonstrates hierarchical and multiscale features (Marieb and Keller, 2018; Martini et al., 2012). The duodenum, for example, is a 25-cm-long cylindrical tube with a diameter of 4 cm (Martini et al., 2012). Plicae circularis (i.e., circular folds) – submucosa protrudes with a maximum height of about 8 mm – are distributed along the inner wall of the tube (Standring, 2008). The surface of the circular folds is covered with finger-like bumps, referred to as villi. The height of a villus is only around 1 mm. In addition, micrometer-scale microvilli form a brush border on the villi surface. The microvilli secrete specific enzymes to enable the digestion of carbohydrates and proteins (Hall, 2016).

It has been widely accepted that this multiscale structure can drastically increase the absorption area (Martini et al., 2012). Nevertheless, whether these structures can contribute to digestion and absorption, other than to increasing the area, has not yet been rigorously investigated. From the chemical engineering perspective, nutrient molecules need to overcome mass transfer resistance in the lumen (i.e., cavity within the tube) before their arrival at the villi surface where the absorption takes place. The intestinal wall movement drives fluid convection and mixing in the lumen, effectively reducing mass transfer resistance and, hence, positively contributing to digestion and absorption. It will be interesting and meaningful to investigate whether the structure of the intestinal inner wall can lead to mixing intensification. If the answer is yes, then how much intensification can be achieved? This study was motivated by this scientific question, with the aim of quantitatively revealing the role of circular folds in mixing intensification.

Many experimental and simulation efforts have been devoted to the study of the small intestine. Intestinal motility causes chyme to mix with intestinal secretions, and the measurement of motion patterns began as of 1899 and perhaps even earlier. Researchers at the time used a graphic method and discovered a number of intestinal movements (Bayliss and Starling, 1899). The two major ones are segmentation movement (i.e., mixing contraction) and peristalsis (i.e., propulsive contraction). The 3rd type is pendular movement (i.e., longitudinal contraction) (Lentle and Janssen, 2011), which is not well-known. The segmentation, as opposed to peristalsis, was observed to be the main form of movement during the post-prandial period since residence time values should be longer than the time needed to achieve acceptable mixing (Husebye, 1999; Lentle and de Loubens, 2015; Sarna et al., 1983). The real-time motion of the intestinal tract can be illustrated using

spatiotemporal maps (Lentle and de Loubens, 2015). Tremendous efforts have been made as well to characterize the physical and chemical properties of the gastrointestinal contents and intestinal structures. Extensive measurements have been made of the length and width of the intestine, the viscosity of the chyme, the amplitude and frequency of the contraction wave, etc. These valuable data provide a solid base for the further study of the gastrointestinal tract (Bornhorst et al., 2013; de Loubens et al., 2013; Lentle et al., 2013). However, these costly *in vivo* studies are always subject to ethical constraints and require the sacrifice of animals. It is extremely challenging, if not impossible, to produce live experimental subjects that have specifically-designed intestinal structures. In this regard, *in vitro* models (i.e., experimental prototypes) are promising alternatives and have received increasing attention in recent years. These efforts include near-real *in vitro* digestive systems for rats and humans developed by Chen et al. (Chen et al., 2016; Deng et al., 2014; Wu et al., 2017a, 2017b; Zhang et al., 2018), and a dynamic duodenal model developed by Gouseti et al. (Gouseti et al., 2014, 2019). However, considering detailed hierarchical structure on the organ surface in such *in vitro* investigations is still a very challenging task. Moreover, collecting comprehensive real-time process data is always limited by the capability of existing experimental techniques.

In order to better capture the intestinal flow behavior and the mixing of gastrointestinal content, numerical simulation has played an increasingly important role in the study of the gastrointestinal tract in recent years. Through simulation, intestinal motility can be flexibly implemented, and local changes in the properties of intestinal contents, such as viscosity and density, can be characterized. For example, Sinnott et al. (2012, 2017) used the smoothed particle hydrodynamics (SPH) method and the fluid-solid coupling method to study the transport of matter in the duodenum or colon. They reported that both the content viscosity and the degree of occlusion of the cavity play an important role in the transport of intestinal contents. In 2014, de Loubens et al. investigated the mixing process in the proximal duodenum of rat under longitudinal contraction. The results showed that longitudinal contraction had a more significant effect on mixing in the near-wall region than in the central region of the intestinal cavity. Fullard et al. (2014, 2015) compared systems with different fluid properties and found that the mixing effect of segmental contraction was more significant for fluid with a higher viscosity, whereas longitudinal contraction promoted species transport in the near-wall region only. In addition to the investigation of intestinal motility and chyme properties, the transport of bacteria in the intestine has also been studied by numerical simulations (Ishikawa et al., 2011), where the effects of peristalsis on the distribution of anaerobic and aerobic bacteria in the presence of oxygen and nutrients were analyzed.

Without exception, the simulation efforts mentioned above depicted the intestine as a smooth tube, which is far from mimicking its complex hierarchical structure. It remains unclear whether the hierarchical structure of the intestinal inner surface can contribute to mixing intensification or not. Rather than simulating the whole duodenum, some researchers instead focused on a small section of it, which allowed them to study part of the detailed structure. Lim et al. (2015) used a Lattice Boltzmann Method (LBM) to simulate fluid flow and absorption for a very small section of the duodenum that contains only five villi. The same system was further investigated by Hua et al. (2020) using a CFD model, where the distribution of absorption flux along the villi surface can be quantified. They found that mass transfer and, hence, absorption can be enhanced due to the villi movement. In 2020, Zhang et al. investigated a relatively larger system, i.e., a rat duodenum, with consideration of the villi structure. Mass transfer and absorption under the pendular movement were simulated and analyzed by a

CFD model. The success of this work verified that it's feasible to model the intestinal wall movement by the moving mesh method. These preliminary efforts demonstrate the role of the intestinal inner surface structure in promoting mass transfer in the lumen. However, compared to the rat system, the human duodenum is much larger and features large circular folds in addition to small villi and microvilli. New numerical models need to be developed for the human intestinal system.

In this study, a multiphysics model was developed to simulate mixing in a virtual human duodenum under the segmentation contraction, which was implemented and solved using Ansys Fluent. A unique feature of the model is that it takes account of the circular folds on the intestinal inner surface, whose movement takes place through a moving mesh method. It should be pointed out that the objective of this work is not to simulate the digestion process in a real small intestine, which has a very complex structure. Instead, the role of the circular folds in promoting mass transfer in the lumen will be explored. It is an essential first step towards a comprehensive understanding of the role of the special multiscale structure of the inner intestinal wall in the process of digestion. After the methodology section, comparisons between the system with and without circular folds are presented, quantitatively demonstrating the role of folds in mixing intensification. At the same time, parametric analyses have been conducted that include the study of the geometry of the folds and the amplitude, frequency and wavelength of contractions. The insights obtained from the simulation and analysis allow us to understand the digestion process in the human body. At the same time, they offer guidance for the improved design of bio-inspired soft elastic reactors (Liu et al., 2018a,b), whose mixing efficiency must be improved for potential industrial applications (Delaplace et al., 2018, 2020; Li et al., 2019; Xiao et al., 2018; Zhang et al., 2019; Zou et al., 2020).

## 2. Modeling and analysis methods

### 2.1. Geometrical construction

The duodenum can be represented as a tube with a pre-specified length ( $L$  (m)) and diameter ( $2R_0$  (m)) (see Fig. 1(a)). Since the system is axial symmetric, a 2D axisymmetric model was developed (see the cross-sectional view in Fig. 1(a)). The circumferential gradient was neglected. According to the anatomy data, the distance from the pylorus to the location of the first fold is  $a$  (m). The folds are uniformly distributed throughout the remaining part of the duodenum with a distribution density  $\omega$  (folds/m). Truncated sinusoidal waves are used to represent the shape of the folds. Each fold has a height of  $h_f$  (m) and a width of  $w_f$  (m) (Fig. 1(a)). A ratio  $\xi$  is defined to characterize the fold geometry:

$$\xi = \frac{h_f}{w_f} \quad (1)$$

The distance between two adjacent folds can be calculated as:

$$2z_0 = \frac{1}{\omega} - w_f \quad (2)$$

Moreover, truncated circles with a radius of  $r_f$  (m) are used to smoothly connect adjacent folds. The radius can be calculated as:

$$r_f = \frac{z_0 \cdot w_f}{\pi h_f} \sqrt{\left(\frac{\pi h_f}{w_f}\right)^2 + 1} \quad (3)$$

The derivation steps of this radius are given in detail in the Appendix A.

The above-described system is constructed on the basis of the physiological data of a real human duodenum. In the following text, this system is denoted as "System 1", or "tube with folds".

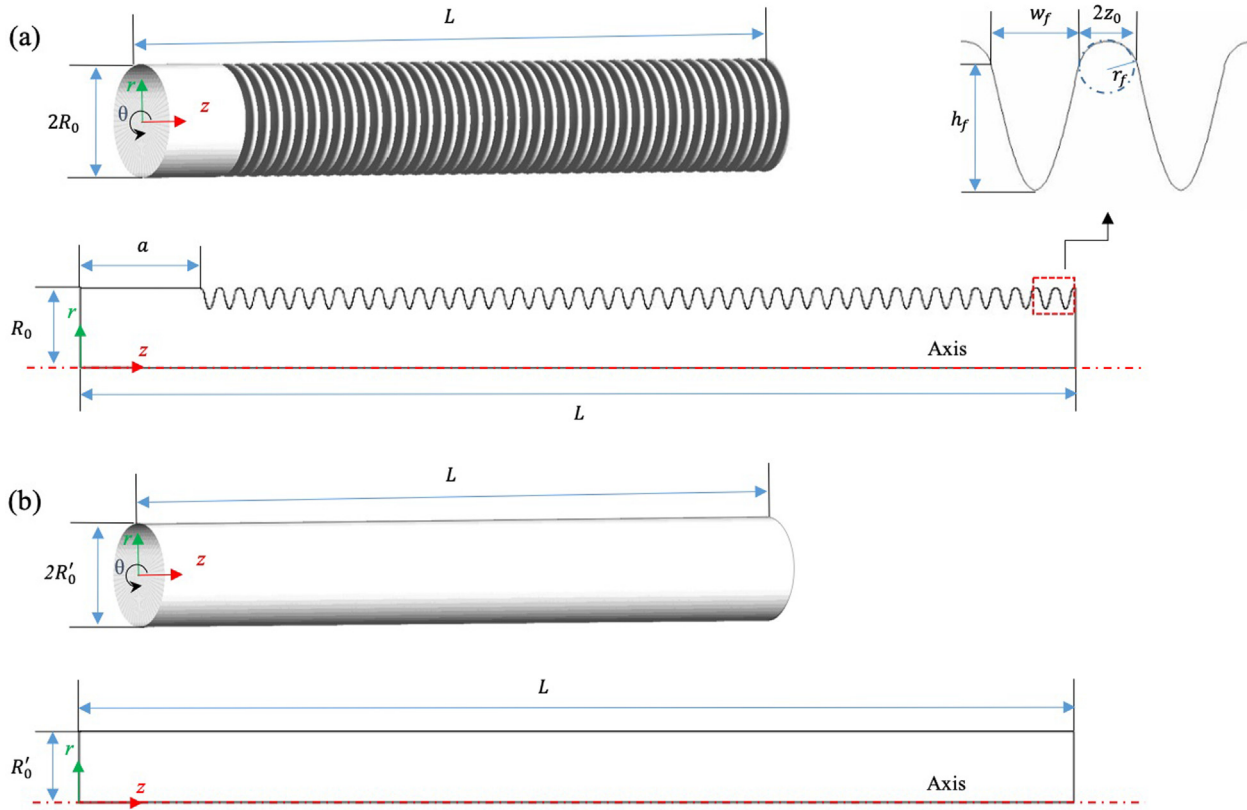


**Fig. 1.** Comparison of the two systems under investigation: (a) System 1: a duodenum with circular folds; and (b) System 2: a duodenum without circular folds.

In order to clearly identify the role of folds in the mixing process, a smooth tube was also designed. This system is denoted as “System 2”, or “tube without folds” (see Fig. 1(b)). For a fair comparison, it was chosen to maintain constant the length and the volume of the two systems. Since the volume of System 1 is  $\int_0^L \pi R^2 dz$ , and the volume of System 2 is simply  $\pi R_0'^2 L$ , the radius of System 2 has to satisfy:

$$R'_0 = \sqrt{\frac{\int_0^L R^2 dz}{L}} \quad (4)$$

where  $R$  is the radius of the non-smooth duodenum, which is a function of the axial position  $z$ . As shown in Fig. 1(a),  $R(z)|_{z=0} = R_0$ .

## 2.2. Governing equations

After digestion by the stomach, the chyme enters the duodenum for further digestion and absorption. It is an extremely challenging task to model solid–liquid–gas three-phase flow coupled with reactions and mass transfer in an evolving geometry with complicated boundary structures. As a first step toward a comprehensive understanding of digestion, this study focuses only on simulating the mixing of dissolved glucose in water.

Momentum transfer. In the small intestine, the flow can be considered as the laminar flow (Lentle and de Loubens, 2015; Lentle and Janssen, 2011). For the mixing study in our case, the fluid is water with dissolved glucose, which is an incompressible fluid. The Navier-Stokes equation is adopted to describe the fluid flow.

$$\frac{\partial \rho}{\partial t} + \nabla \cdot (\rho \mathbf{u}) = 0 \quad (5)$$

$$\frac{\partial}{\partial t}(\rho \mathbf{u}) + \nabla \cdot (\rho \mathbf{u} \mathbf{u}) = -\nabla p + \nabla \cdot (\mu(\nabla \mathbf{u} + (\nabla \mathbf{u})^T)) - \frac{2}{3}\mu(\nabla \cdot \mathbf{u})\mathbf{I} \quad (6)$$

where  $\rho$  is the fluid density ( $\text{kg}/\text{m}^3$ );  $\mathbf{u}$  is the velocity vector ( $\text{m}/\text{s}$ );  $p$  is the fluid pressure ( $\text{Pa}$ );  $\mu$  is the Newtonian fluid viscosity, ( $\text{Pa}\cdot\text{s}$ ); and  $\mathbf{I}$  is the unit tensor.

Mass transfer. The mass fractions of glucose and water are calculated by the species transport equation shown below:

$$\frac{\partial}{\partial t}(\rho Y_i) + \nabla \cdot (\rho \mathbf{u} Y_i) = -\nabla \cdot \mathbf{J}_i \quad (7)$$

$$\mathbf{J}_i = -\rho D_{i,m} \nabla Y_i \quad (8)$$

where  $Y_i$  is the mass fraction of species  $i$ ;  $\mathbf{J}_i$  is the diffusive flux of species  $i$  ( $\text{kg}/(\text{m}^2\cdot\text{s})$ ); and  $D_{i,m}$  is the mass diffusion coefficient for species  $i$  in the binary mixture ( $\text{m}^2/\text{s}$ ). In this study, the dissolved species  $i$  is glucose. The mixture density is location and time dependent and can be calculated based on the volume weighted mixing law:

$$\rho = \nu_g \cdot \rho_g + (1 - \nu_g) \cdot \rho_w \quad (9)$$

$$\nu_g = \frac{c_g \cdot M_g}{\rho_g} \quad (10)$$

where  $\nu_g$  is the volume ratio of the glucose;  $\rho_g$  is the glucose density ( $\text{kg}/\text{m}^3$ );  $\rho_w$  is the water density ( $\text{kg}/\text{m}^3$ );  $c_g$  is the concentration of glucose ( $\text{mol}/\text{m}^3$ ); and  $M_g$  is the molecular weight of glucose ( $\text{g}/\text{mol}$ ).

### 2.3. Boundary and initial conditions

The boundary and initial conditions adopted in the simulations are shown in Fig. 2.

In this study, the aim was to reveal the role of circular folds in mixing. In reality, the chyme requires a certain residence time for mixing and absorption in the duodenum. Thus, a closed system without mass exchange with the up-stream stomach and the down-stream jejunum has been adopted. Nutrient absorption through the intestinal inner wall was not considered. Non-slip and no-flux boundary conditions are applied to all boundaries except the central axis (see Fig. 2). The glucose solution was introduced into the system through DEFINE\_INIT UDF. The shaded elliptic region was filled with glucose solution of a specific initial concentration,  $c_0$ . The remaining space was filled with water only. For an axisymmetric system, only half of the cross-section of the duodenum needs to be simulated.

The geometry of the duodenum evolves over time, and segmentation is the main form of intestinal motility responsible for mixing. The segmentation contraction divides the intestine into a number of sections, i.e., a wave-like movement. As shown in Fig. 3(a), when one set of contractions relaxes, a new set of contractions begins. Contraction and relaxation occur sequentially and alternatively at the same location (Hall, 2016). In order to conserve the mass, the expansion part and the contraction part of the wave have the same amplitude (Sherwood, 2011). Taking the part of the wave indicated by the blue arrow in Fig. 3(a), for example, contraction occurs from 0 to  $T/4$ , followed by relaxation from  $T/4$  to  $3T/4$ , where  $T$  is the cycle period. In the final stage of this cycle (i.e., from  $3T/4$  to  $T$ ), it contracts again. The dashed red rectangle in Fig. 3(a) indicates a repeating unit of the sinusoidal wave. If the wavelength is 0.07 m (as in Wright et al., 2016), then there are three repeating units in the base case. Fig. 3(b) illustrates the relaxation area and contraction position, which will be used in the remaining text.

Mathematically, the contraction wave is represented by a sinusoidal wave. For the smooth tube (i.e., System 2 in Fig. 3(b)), the displacement of the lumen wall can be written as:

$$P(z) = -\delta \cdot \sin\left(\frac{2\pi}{\lambda}(z - b)\right) \quad (11)$$

$$\delta = \varepsilon^* \cdot R_c \quad (12)$$

where the amplitude and length of the wave are  $\delta$  (m) and  $\lambda$  (m), respectively (see Fig. 3). The contraction starts at  $b$  (m) from the pylorus.  $\varepsilon^*$  gives the ratio between the wave amplitude and the tube radius.  $R_c$  (m) is the characteristic radius of the lumen, which is  $R'_0$  in the base case. In order for the geometry to evolve over time, the following term is introduced:

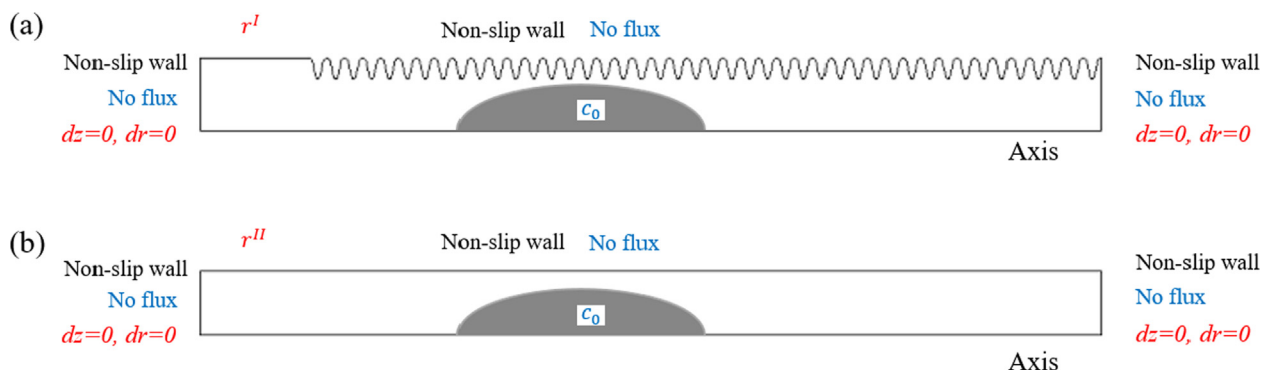


**Fig. 2.** Initial and boundary conditions for two systems: (a) System 1; and (b) System 2. The black, blue and red fonts refer to momentum transfer, mass transfer and moving mesh, respectively. (For interpretation of the references to colour in this figure legend, the reader is referred to the web version of this article.)

$$\Gamma(t) = \sin(2\pi ft) \quad (13)$$

where  $f$  is the frequency of segmentation (cycles/min). The position of the lumen wall is then:

$$r^{II} = R'_0 + P(z) \cdot \Gamma(t) \quad (14)$$

For System 1 in Fig. 3(a), the segmentation movement takes the circular folds into account. The position deviation from a smooth tube due to the folds can be written as:

$$F(z) = \begin{cases} 0, & \text{when } z \in [0, a] \\ \sqrt{r_f^2 - (z - (a + 2(n-1)z_0 + (n-1)w_f))^2} - r_f, & \text{when } z \in (a + (2n-3)z_0 + (n-1)w_f, a + (2n-1)z_0 + (n-1)w_f] \cap (a, L) \\ (\sqrt{r_f^2 - z_0^2} - r_f) - h_f \cdot \sin\left(\frac{\pi}{w_f}(z - (a + (2n-1)z_0 + (n-1)w_f))\right), & \text{when } z \in (a + (2n-1)z_0 + (n-1)w_f, a + (2n-1)z_0 + w_f] \cap (a, L) \end{cases} \quad (15)$$

where  $n$  is the index of the circular folds. Detailed derivation of Eq. (15) has been given in Appendix B. The shape of the folds is assumed to be unchanged during the segmentation movement (Marieb and Keller, 2018; Martini et al., 2012). The evolution of the lumen wall position can be written as:

$$r^I = R_0 + F(z) + P(z) \cdot \Gamma(t) \quad (16)$$

Eqs. (16) and (14) are the boundary conditions in the moving mesh model for the lumen walls of System 1 and System 2, respectively (see Fig. 2). The locations of all other boundaries remain unchanged during the simulation.

### 2.4. Quantification of mixing performance

The Reynolds number is calculated to describe the flow regime:

$$Re = \frac{2R_c u_c \rho_c}{\mu} \quad (17)$$

where  $u_c$  is the characteristic velocity, i.e., the volume-averaged velocity in the intestinal lumen (m/s):

$$u_c = \frac{\int |\mathbf{u}| dV}{\int dV} \quad (18)$$

$\rho_c$  is the volume-averaged density:

$$\rho_c = \frac{\int \rho dV}{\int dV} \quad (19)$$

To find out the dominant mechanism of mass transfer, the Peclet number is quantified as:

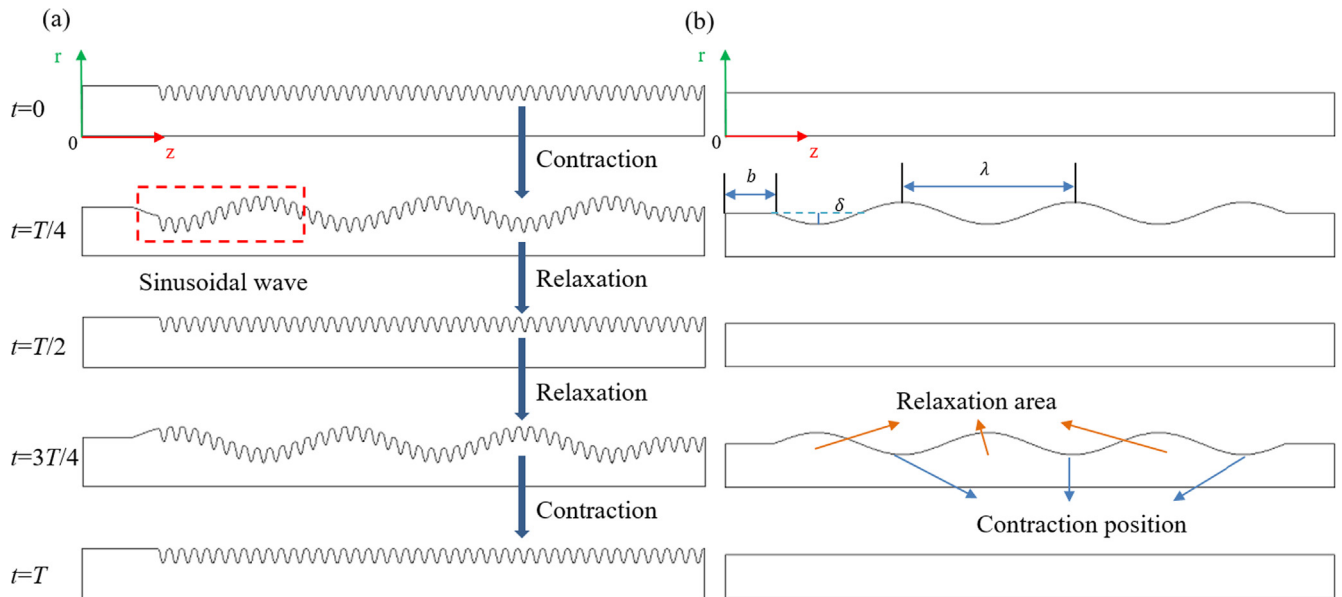


**Fig. 3.** Illustration of one cycle of the segmentation movement: (a) System 1; and (b) System 2.

$$Pe = \frac{2R_c u_c}{D} \quad (20)$$

An ideally mixed state is a state when the glucose molecules are homogeneously distributed in the lumen. This means that the glucose concentration becomes a constant,  $c_\infty$  (mol/m<sup>3</sup>), which is the average volume concentration:

$$c_\infty = \left. \frac{\sum_{j=1}^N (c_{j,t} \cdot V_{j,t})}{\sum_{j=1}^N (V_{j,t})} \right|_{t=0} \quad (21)$$

where  $c_{j,t}$  and  $V_{j,t}$  are the concentration and volume of the  $j^{\text{th}}$  volume element, respectively. The total volume is divided into  $N$  mesh elements. A mixing level of each mesh element can be defined based on the concentration deviation from the average concentration  $c_\infty$ .

$$\chi_{j,t} = \begin{cases} \frac{c_{j,t}}{c_\infty}, & \text{for } c_{j,t} \leq c_\infty \\ \frac{c_0 - c_{j,t}}{c_0 - c_\infty}, & \text{for } c_{j,t} > c_\infty \end{cases} \quad (22)$$

Note that at different locations, the concentration may be higher or lower than the average concentration.

The overall mixing level at  $t$  for the whole system can then be calculated as:

$$\chi(t) = \frac{\sum_{j=1}^N (\chi_{j,t} \cdot V_{j,t})}{\sum_{j=1}^N (V_{j,t})} \quad (23)$$

which essentially offers a volume average of the mixing level values in all volume elements. An enhancement ratio is defined as:

$$\alpha(t) = \frac{\chi^I(t)}{\chi^{II}(t)} \quad (24)$$

where the superscripts  $I$  and  $II$  represent system 1 (with folds) and system 2 (without folds) respectively. This ratio quantifies the enhancement of mixing level as a function of time due to the introduction of the circular folds.

## 2.5. Simulation settings

The meshing and simulation were carried out using ANSYS Fluent software. For transient calculations, PISO was used as the present

sure-velocity coupling algorithm. In order to obtain a stable moving mesh calculation, automatic remeshing was adopted. The residual of velocity was set to  $1 \times 10^{-4}$ , and the residual of mass fraction was specified as  $1 \times 10^{-6}$ . The time step for System 1 was set to 0.005 s due to its relatively complicated geometry, whereas the value was 0.01 s for System 2. Under these settings, the convergence condition could be met between 5 and 10 iterations in each time step. The local cell remeshing method was adopted. The mesh was reconstructed at every time step when cells marked for remeshing were detected. Cells were marked based on skewness and size.

## 2.6. System specifications

The settings for the duodenum geometry and contraction movement are based on the physiological data. The dissolved nutrient for the mixing study in our case is glucose. The initial elliptic region filled with glucose solution is specified by:

$$\frac{(z - 0.1075)^2}{0.035^2} + \frac{r^2}{0.014^2} \leq 1 \quad (25)$$

The values used in the base case simulation are listed in Table 1. The property values at the body temperature, i.e., 37 °C, were adopted. The segmentation contraction occurs during digestion (Barrett et al., 2016), but the continuous and rhythmic contractions are generally maintained for a short time (Cannon, 1902). It is not common to have more than seven consecutive contractions (Macagno and Christensen, 1980). Since the frequency of intestinal contractions used in this work is about 6–12 cycles per minute, the simulation time was chosen as 1 min, i.e., 60 s, so that one set of consecutive contractions can be simulated.

In addition to the base case, 22 additional cases were designed for a parametric study. To facilitate comparison and discussion, all of the cases are organized as a number of case sets, whose settings are listed in Table 2. For example, case set 1 has four cases with the same value of  $f$  (i.e., 6 cycles/min) but different  $c^*$ . All other parameters not listed in Table 2 have the base case values given in Table 1. Note that Set 1 to Set 8 actually have a total of 16 cases, and the base case is one of them. Also, for Set 3, Set 6, Set 9 and Set 10, each of them contains one base case. Moreover, for each case in Set 1 to Set 9, two simulations are conducted: one for System 1 and the

**Table 1**

Parameter values used in the base case simulation.

Parameters		Notation	Value	References
Duodenum tube	Length	L	0.25 m	(Martini et al., 2012)
	Radius	R <sub>0</sub>	0.02 m	(Martini et al., 2012)
Circular folds	Height	h <sub>f</sub>	0.005 m	(Helander and Fandriks, 2014; Standring, 2008)
	Width	w <sub>f</sub>	0.003 m	(Krag, 1966)
	Distribution density	ω	200 folds/m	(Martini et al., 2012)
	Distance from pylorus to the 1st fold	a	0.03 m	(Standring, 2008)
Segmentation contraction	Amplitude to radius ratio	ε*	25%	(de Loubens et al., 2013; Fullard et al., 2015)
	frequency	f	10 cycles/min	(Hall, 2016; Martini et al., 2012)
	wavelength	λ	0.07 m	(Wright et al., 2016)
Glucose	Diffusion coefficient	D	8.97 × 10 <sup>-10</sup> m <sup>2</sup> /s	(Zhang et al., 2020)
	Density	ρ <sub>g</sub>	1540 kg/m <sup>3</sup>	<a href="https://en.wikipedia.org/wiki/Glucose">https://en.wikipedia.org/wiki/Glucose</a>
	Molecular weight	M <sub>g</sub>	180.156 g/mol	<a href="https://en.wikipedia.org/wiki/Glucose">https://en.wikipedia.org/wiki/Glucose</a>
Glucose solution	Initial concentration	c <sub>0</sub>	200 mol/m <sup>3</sup>	(Leiper, 2015)
	Viscosity	μ <sub>g</sub>	0.6913 mPa·s	<a href="https://wiki.anton-paar.com/en/water/">https://wiki.anton-paar.com/en/water/</a>
	Density	ρ	Eq. (9)	(Zuo et al., 2016)
Water	Density	ρ <sub>w</sub>	993.3 kg/m <sup>3</sup>	<a href="https://wiki.anton-paar.com/en/water/">https://wiki.anton-paar.com/en/water/</a>
	Viscosity	μ <sub>w</sub>	0.6913 mPa·s	<a href="https://wiki.anton-paar.com/en/water/">https://wiki.anton-paar.com/en/water/</a>
	Molecular weight	M <sub>w</sub>	18.01528 g/mol	<a href="https://www.webqc.org/molecular-weight-of-water.html">https://www.webqc.org/molecular-weight-of-water.html</a>

**Table 2**

Settings for the parametric study.

Parameters		Index of case set	Value	Notes
Segmentation contraction	f (cycles/min)	Set 1	6	ε* = 5%, 25%, 45%, 65% f (cycles/min) = 6, 8, 10, 12
		Set 2	8	
		Set 3	10	
		Set 4	12	
	ε*	Set 5	5%	
		Set 6	25%	
		Set 7	45%	
		Set 8	65%	
	λ(cm)	Set 9	3, 5, 7, 9	
		Set 10	(3, 3), (4, 3), (5, 3), (5, 2), (5, 4)	Base case settings for others Base case settings for others
Size of folds	(h <sub>f</sub> , w <sub>f</sub> ) (mm)			

other for System 2. In this way, the effects of fold geometry and segmentation contraction on mixing can be systematically investigated.

### 2.7. Mesh independence study

Mesh independence studies were conducted for System 1 and System 2. Five different meshes were tested for each system (see Fig. 4). Unstructured triangular mesh was used. The geometrical parameters of System 1 are specified in Table 1. The radius of the smooth tube in System 2 can be calculated using Eq. (4).

The distributions of velocity magnitude and concentration along the central axis at the final moment of calculation (60 s) are plotted in Fig. 5. Furthermore, in the same figure, the evolution of mixing level throughout the process is also given. For System 1, when the number of mesh elements reaches 110,028 and beyond, differences between results under different meshes may be neglected (see Fig. 5(a)). Thus, the 4th mesh in Fig. 4(a) was used for System 1. For System 2, clear differences exist only for the mixing level curves under different meshes with less than 102,602 elements (Fig. 5(b-3)). Thus, the 4th mesh in Fig. 4(b) was adopted for the simulation of System 2.

## 3. Results and discussion

### 3.1. Base case analysis

The evolution of velocity fields with streamlines in one segmentation movement cycle for both systems is plotted in Fig. 6 for

comparison. Taking System 1 as an example (Fig. 6(a-1)), for the first half of the cycle (i.e., t = 0 to T/2), the wall begins to deform from the initial state. The fluid reveals an overall rightward flow, where the direction is indicated by the arrows on the streamline and the thick red arrows (see Fig. 6(a-1) at t = 1.2 s). This phenomenon is mainly due to the specific shape of the segmentation wave implemented in this case, for which the contraction positions are on the left side of the relaxation areas. The fluid near the contraction position is pushed towards the relaxation area. Since the system is closed, a reflux is inevitable. As the wall continues to deform, a clockwise vortex begins to form close to the end of the duodenum at t = 1.3 s (see Fig. 6(a-1)). After that, the number and size of vortices grow over time. The peak values are reached at 1.5 s (i.e., T/4), when the duodenum reveals a maximum deformation and eight big vortices can be observed.

During the shape recovery stage from T/4 to T/2, most vortices gradually become smaller and eventually disappear. The original relaxation areas experience contraction, which pushes the liquid back to the original contraction areas that are new relaxation areas. As a consequence, the flow direction is reversed, pointing toward the left side in Fig. 6(a-1) at T/2.

For the next quarter of the cycle (from T/2 to 3T/4), the recovered shape begins to deform again, but this time, toward the opposite direction. The number and size of vortices in the lumen increase again until the time of maximum deformation at 3T/4. The final quarter of the cycle is the 2nd shape-recovery stage, when most of the vortices become smaller and eventually disappear. The overall flow direction reverses back again (see Fig. 6(a-1) at T).

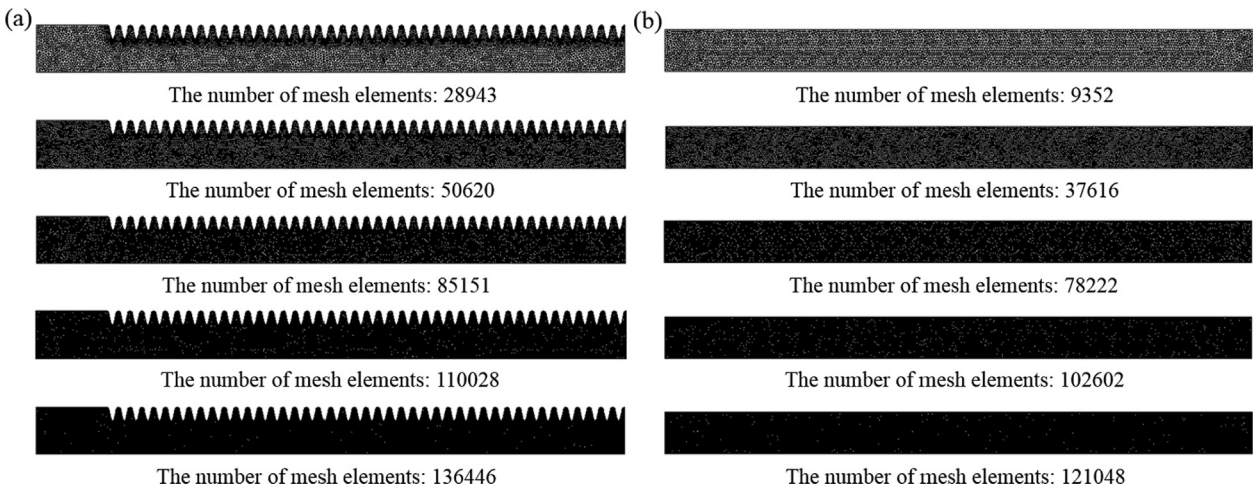


**Fig. 4.** Different meshes designed for the mesh independence study: (a) System 1; and (b) System 2.

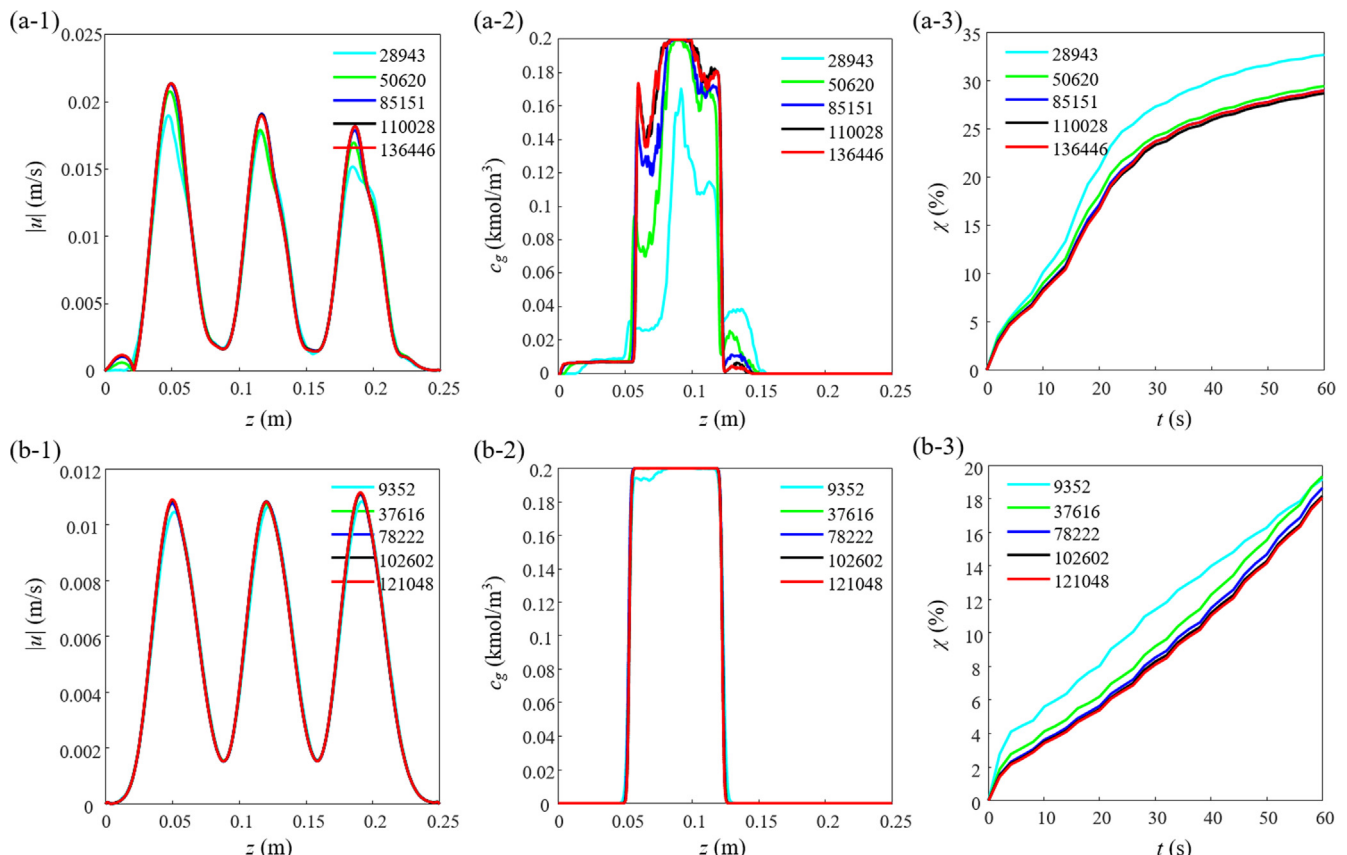


**Fig. 5.** Results obtained for systems with different meshes: (a) System 1; and (b) System 2. (a-1) and (b-1) are the distribution of velocity magnitude along the axis of symmetry at 60 s; (a-2) and (b-2) are the distribution of molar concentration of glucose along the axis of symmetry at 60 s; (a-3) and (b-3) show the evolution of mixing level as a function of time.

This cyclic process of deformation-recovery-deformation-recovery occurs in the following cycles of the segmentation movement. The resulting back and forth flow, together with local vortices, promotes axial and radial mixing of fluids in the lumen. As shown in Fig. 6(a-1) and (b-1), both of the systems experience the same deformation and recovery. The flow pattern and its evolution are very similar. Vortices form and grow in the deformation stage, whereas they gradually diminish and even disappear in the recovery stage. At the end of the deformation stage (i.e., the state of

maximum deformation at  $T/4$  and  $3T/4$ ), the most prominent vortices can be identified. The duodenum recovers its original shape at the end of the recovery stage (i.e.,  $T/2$  and  $T$ ) when the velocity of the fluid in the lumen reaches a peak value in one cycle.

The differences in flow fields between the two systems can be seen in Fig. 6(a-1) and (b-1), where both of them have the same color bar. Compared with the smooth tube, the system with circular folds provides: (1) greater velocity in the lumen; and (2) more prominent vortices with a longer life cycle. The higher velocity of

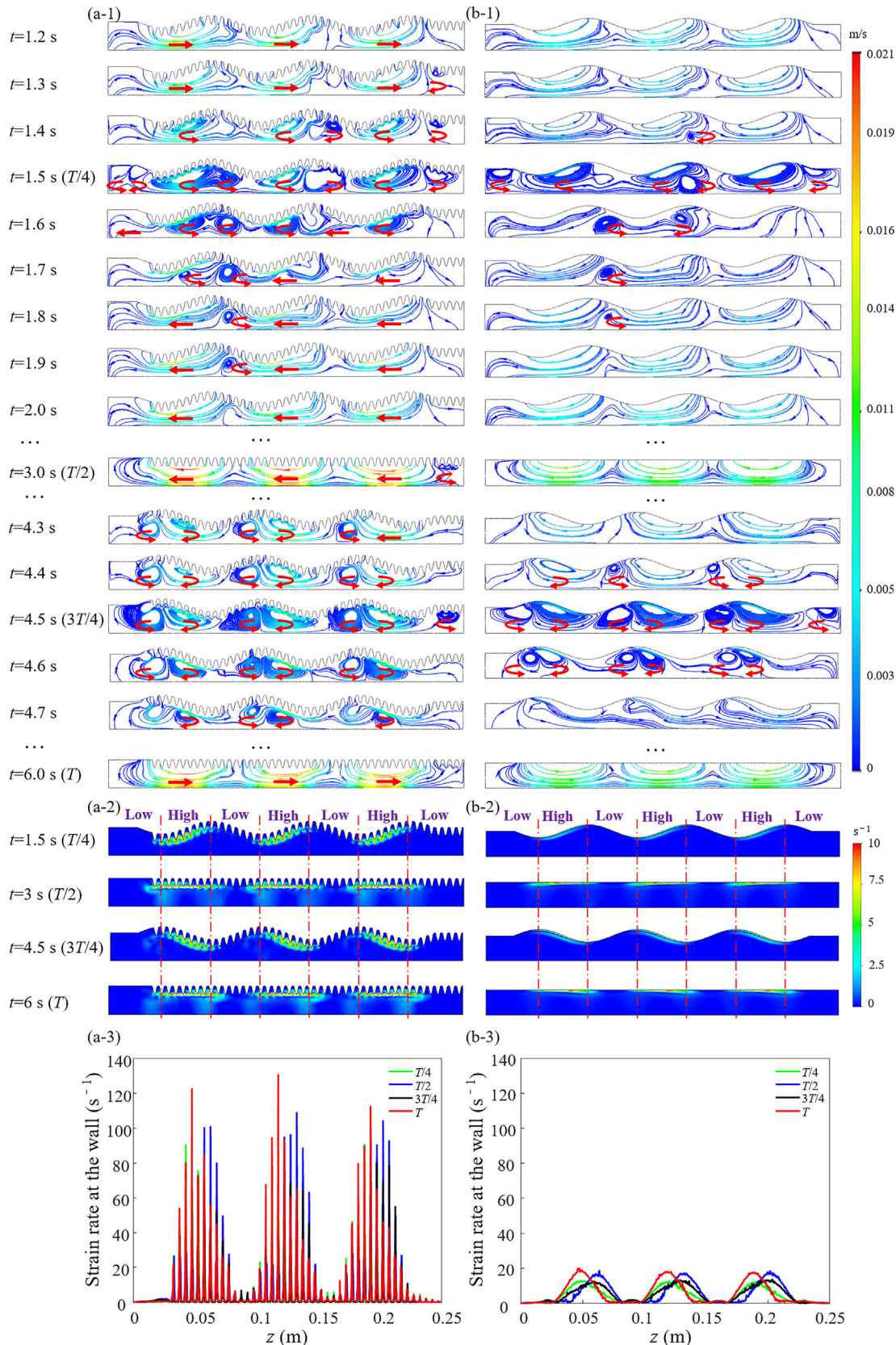


**Fig. 6.** Evolution of the velocity field with streamlines and strain rates in one segmentation cycle: (a) System 1; and (b) System 2. Shear rates at the wall at four representative time instants are given in (a-3) and (b-3). To facilitate the comparison, both systems share the same color bar. Streamlines with arrows are colored based on the velocity magnitude. Thick red arrows have been added to show the flow direction. The strain rate in this study is the shear rate that links the shear stress to the Newtonian viscosity. Strain rate values higher than  $10 \text{ s}^{-1}$  are not plotted in (a-2). Dotted red lines are used to differentiate the zones with "High" or "Low" shear rates.

fluid in System 1 can be seen by comparing the color of the streamlines in both sets of subplots. This is mainly due to the reduction of free-flowing space in System 1. Streamlines can be barely identified in the cavities between adjacent protrudes (see the folded regions in Fig. 6(a-1)), indicating that the fluid cannot flow freely in those cavities. Smaller free-flowing space leads to higher fluid velocity. More vortices can be observed in System 1. In the first half of one cycle (0 to  $T/2$ ), the vortices last from 1.3 s to 1.9 s for System 1 (Fig. 6(a-1)), whereas vortices can only be observed from 1.4 s to 1.8 s (Fig. 6(b-1)) for System 2. In the segmentation movement process, the diameter of the lumen channel changes along the axial direction. For both systems, the contraction positions offer the smallest diameter. In System 1, the protrusion of the folds located at the contraction position make the channel even narrower. The relaxation area between two adjacent contraction positions thus forms a relatively closed space, which is beneficial for the formation and growth of vortices. Moreover, the protrudes distributed along the wall become obstacles for fluid flow, which also contributes to vortex formation.

It can be observed that, for both systems, the strain rate near the wall surface is greater than that in the lumen (see Fig. 6(a-2) and (b-2)). It is also interesting to observe that low and high stain rate zones are alternately and regularly distributed along the wall. The high strain rate zone exists in the middle section of one complete cycle of the segmentation wave, taking up about one half of the wavelength. In other words, two adjacent high shear rate zones are always separated by one low shear rate zone that spans approximately half of the wavelength. A higher shear rate indicates a higher velocity gradient, implying a faster mixing. It can thus be assumed that the near-wall region will be better mixed than the central lumen region. The other characteristic pattern can be expected along the axial direction in the lumen. A relatively well-mixed zone and a relatively poorly-mixed zone will be adjacent to each other, each taking up about half a wavelength. Although the contraction positions change over time in one segmentation cycle, the locations of the more well-mixed zones do not change accordingly.

Comparing Fig. 6(a-2) and (b-2), it can be seen that the existence of circular folds provides higher shear rates, implying better mixing performance. The shear stress experienced by a circular fold is not uniformly distributed. The highest shear rate can be identified at the tip of the fold (Fig. 6(a-3)). In System 1, noticeable shear rates can be observed even in the central lumen area, whereas that is not the case for System 2. At  $T/2$  and  $T$ , the shear rates in the central lumen demonstrate a strip pattern with a high shear rate strip next to a low one. Introducing circular folds can enhance the maximum shear rate at the wall by a factor of ~6.5 (Fig. 6(a-3) and (b-3)). Beyond promoting mixing, it is also worthwhile to point out that a higher shear rate indicates a stronger shear stress, which will be especially useful for mechanical breakup of the chyme, i.e., the partially digested food that passes from the stomach into the duodenum. Fig. 6 implies that chyme breakup in the duodenum with circular folds is not restricted to the region close to the wall. This will be further investigated in a future study.

The evolution of the glucose concentration in the 3D lumen for both systems are plotted in Fig. 7 for comparison. The glucose solution is increasingly thoroughly mixed with water over time in the intestinal lumen. It can be observed that mixing occurs mainly in the radial direction rather than the axial direction. Within 10T, the transport of glucose molecules in the axial direction does not seem to be significant (see the area occupied by the glucose molecules). Thus, segmentation movement is mainly for localized mixing rather than axial transport of substances. Circular patterns of concentration can be seen in Fig. 7 (see the subplots at 5T and 10T). This proves that local mixing is driven by vortices. Subplots

at 5T and 10T also show that a relatively better-mixed zone (indicated as "Better") is next to a relatively poorly-mixed zone (indicated as "Worse"). The volume-average mixing level can be obtained for the "better" and "worse" regions. At 10T in Fig. 7, they are respectively 68.73% and 55.07% for system 1, and 61.60% and 40.81% for system 2. These observations are consistent with the analyses on the velocity and shear rate fields.

The mixing performance has been further analyzed. Distributions of localized mixing levels quantified by Eq. (23) are plotted in Fig. 8, side by side with the corresponding glucose concentration distributions at specific moments in time. These 2D hybrid plots are used below to demonstrate the mixing process. The information about localized mixing levels quantified here provides us with the unique opportunity to precisely and quantitatively track the spatial and temporal evolution of mixing. The mixing level plot reveals new findings that cannot be easily identified from the concentration plot. As shown in Fig. 8(a) at 5T and 10T, it is surprising to see that mixing levels reach appropriate values in the areas located on the left side of the zones with a majority of glucose molecules. It can be concluded that axial mixing actually takes place under the segmentation movement in System 1 with circular folds, although radial mixing is still dominant.

The mixing performance in System 1 is better since the distribution of glucose is more homogeneous with a lower concentration gradient (see the comparison between the subplots at 10T in Fig. 7), which can be further confirmed by the mixing level distribution data in Fig. 8. The circular folds can also significantly enhance the axial mixing (see the comparisons between the two systems in Fig. 8 at 5T and 10T). More prominent and long-lasting vortices together with higher strain rates provided by the circular folds in the duodenum play a key role.

The Reynolds number and the Peclet number are further quantified as a function of time for comparison. According to Eqs. (17) and (20), the ratio between  $Re$  and  $Pe$  is a constant (i.e.,  $\frac{ReD}{\mu}$ ), so that one curve can represent both dimensionless numbers in a figure with two different vertical axes, e.g., Fig. 9(a). Since the segmentation contraction is cyclic, the changes in  $Re$  and  $Pe$  within the first cycle are plotted (Fig. 9(a)). For both systems, "W" shaped curves can be observed, with maximum values reached at  $T/2$  and  $T$ , and minimum values reached at  $T/4$  and  $3T/4$ . This is consistent with the analysis of fluid velocity in Fig. 6 since the flow and mixing are driven by the movement of the intestinal wall whose velocity magnitude shows the same pattern within one cycle (see the average velocity magnitude of the wall in Fig. 9(b)). Fig. 9(a) also shows that the Reynolds number in the duodenum is less than 330, confirming the rationality of the laminar flow model. Moreover, the Peclet number is much larger than 1, which indicates the dominant role of convective mass transfer in mixing.

The system with circular folds provides larger values of  $Re$  and  $Pe$  (see Fig. 9(a)), which further leads to enhanced mixing. The overall mixing level at the end of 10T can be significantly increased from 18.20% to 28.76% due to the introduction of circular folds (Fig. 9(c)), which proves the mixing intensification effect of circular folds in the duodenum. The enhancement ratio evolved over time (see Fig. 9(d)). It was increased from 1 to a maximum value (i.e., 3.09) at 22 s. After that, it was gradually decreased to 1.58 at 60 s.

### 3.2. Effects of different amplitudes and frequencies of segmentation on mixing

In the human gastrointestinal tract, the contraction amplitude and frequency of segmentation contraction vary with the property of the food, digestion time, intestinal region, etc. (Takahashi, 2011). The age of the people and their state of health also influence these two parameters. For the intestine, the amplitude of the segmenta-

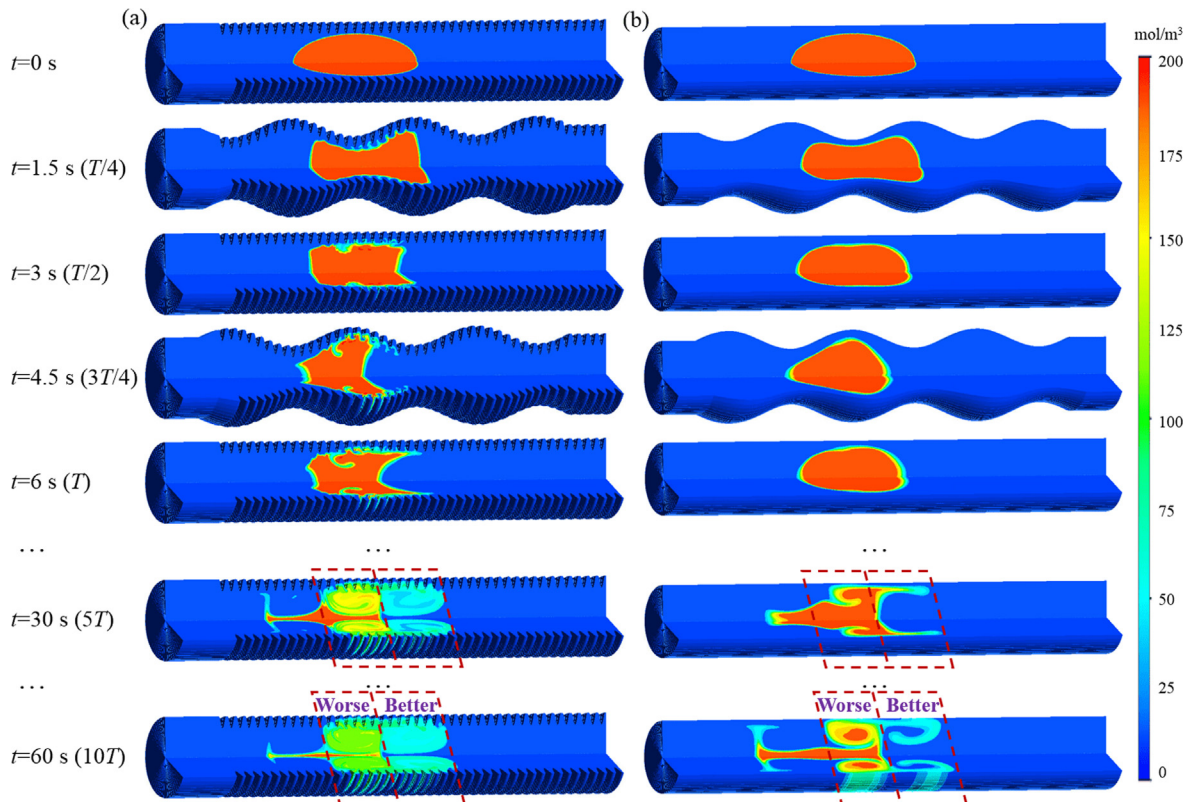


**Fig. 7.** Evolution of concentration fields in 3D: (a) System 1; and (b) System 2. A relatively well-mixed zone (indicated as “Better”) is adjacent to a relatively poorly-mixed zone (indicated as “Worse”).

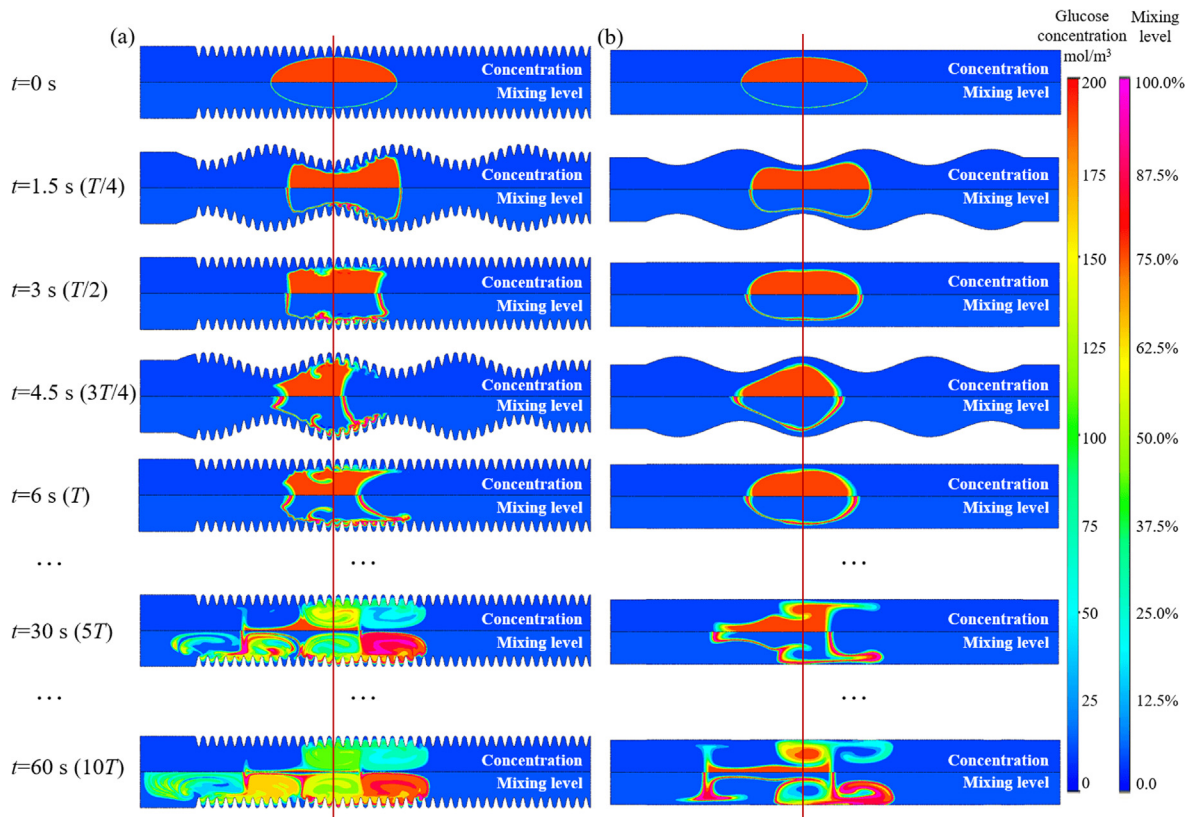


**Fig. 8.** Evolution of concentration fields and mixing level fields: (a) System 1; and (b) System 2. For each hybrid subplot, the top half shows the concentration and the bottom half displays the corresponding mixing level.

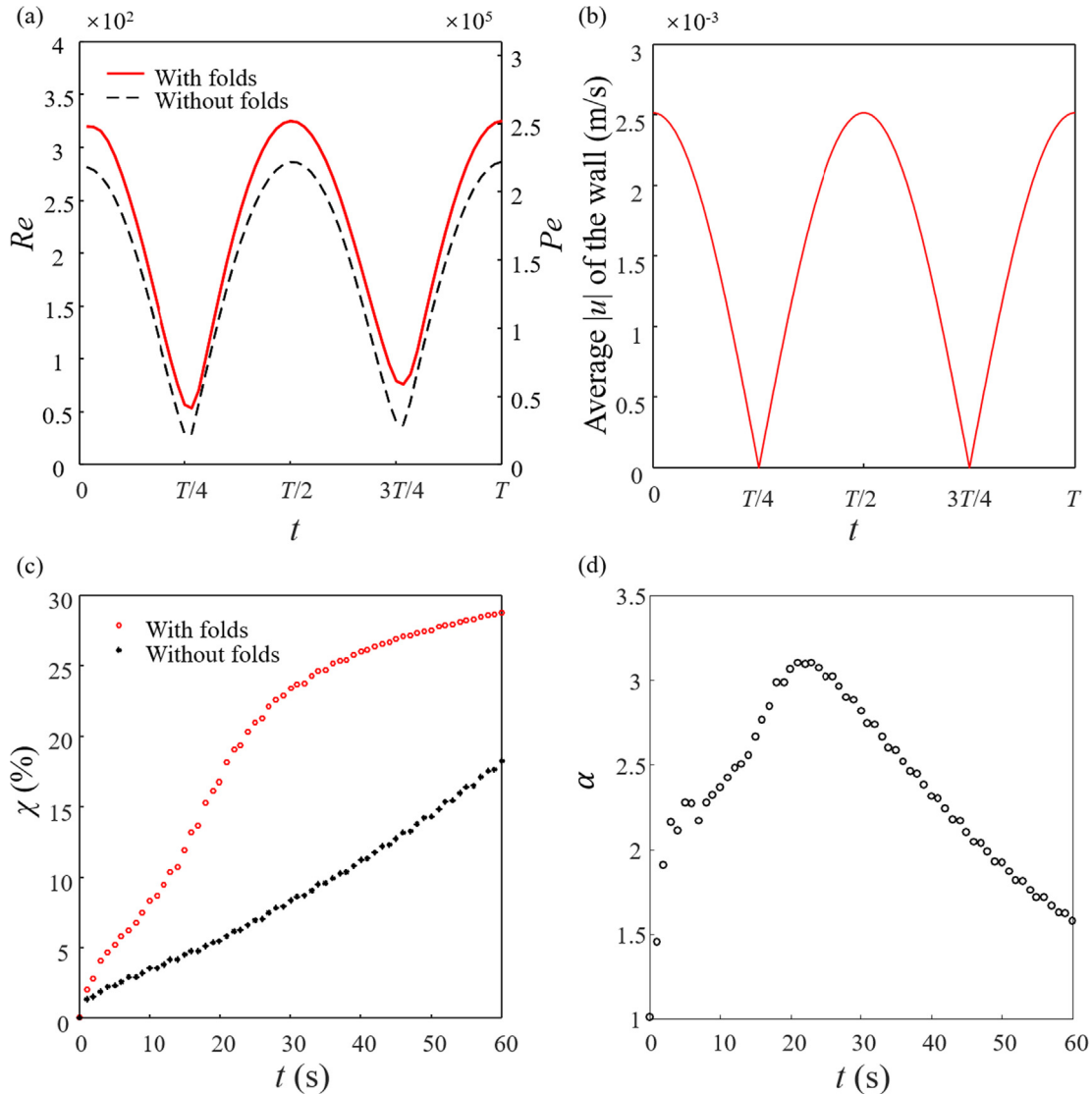


**Fig. 9.** Comparison between the two systems: (a)  $Re$  and  $Pe$  over time in one cycle (i.e., 6 sec); (b) the average of the velocity magnitude of the intestinal lumen wall over time in one cycle (i.e., 6 sec); (c) the overall mixing level as a function of time within  $10T$ ; and (d) the enhancement ratio as a function of time within  $10T$ .

tion contraction in many animals has been observed to be around 25% (de Loubens et al., 2013; Fullard et al., 2015). It is known that the segmentation contraction is very weak and even absent between two meals, but a vigorous motion occurs immediately after a meal (Sherwood, 2011). Thus, amplitudes ranging from a negligible deformation to those almost causing an occlusion of the duodenum were specified for a parametric study. Specifically, values of the amplitude ratio ( $\epsilon^*$ ) under investigation were 5%, 25%, 45% and 65%. In the duodenum, segmentation usually occurs at less than 12 cycles/min, and the maximum frequency is reached only under extreme conditions (Hall, 2016). Frequency values of 6, 8, 10 and 12 cycles/min were therefore chosen for a detailed study. In this section, amplitude ratios varied first under a specific frequency (i.e., Set 1 to Set 4 in Table 2, corresponding to four different frequencies). The frequencies were then changed under a specific amplitude ratio (i.e., Set 5 to Set 8 in Table 2, corresponding to four different amplitude ratios).

The influence of amplitude ratios on mixing under a specific frequency, 10 cycles/min (i.e., Set 3 in Table 2), and the influence of frequencies on mixing under a specific amplitude ratio, 25% (i.e., Set 6 in Table 2), were selected for detailed analyses. For simula-

tions in Set 3, Fig. 10(a-1) and (b-1) show the velocity streamlines at  $T/4$ , i.e., the time of maximum deformation. Taking System 1, for example, when the amplitude ratio is 5%, nine vortices can be identified. With the increase in amplitude ratio, the fluid velocity in the intestinal cavity becomes greater and the number of vortices decreases accordingly. Meanwhile, the relaxation areas become more noticeable. When the ratio reaches 65%, the velocity reaches a maximum value. There are only three prominent vortices, each of which occupies one whole relaxation area, which almost becomes a closed space (see the subplot at  $\epsilon^* = 65\%$  in Fig. 10(a-1)). Fig. 10(a-2) shows the corresponding shear rate distributions at  $T/2$  when the shape reverts to its original state for the first time. The low and high strain rate zones are alternately and regularly distributed, both along the wall and in the lumen. As the amplitude increases, high shear rate zones become more prominent in terms of size and intensity. When the amplitude ratio reaches 65%, just about the entire lumen region exhibits noticeable shear rates, which implies a thorough mixing process.

After 60 s of segmentation contraction (i.e.,  $10T$ ), the distribution of glucose changes compared to the initial state, which is plotted in Fig. 10(a-3) as well (see the subplot at  $t = 0$ ). With an

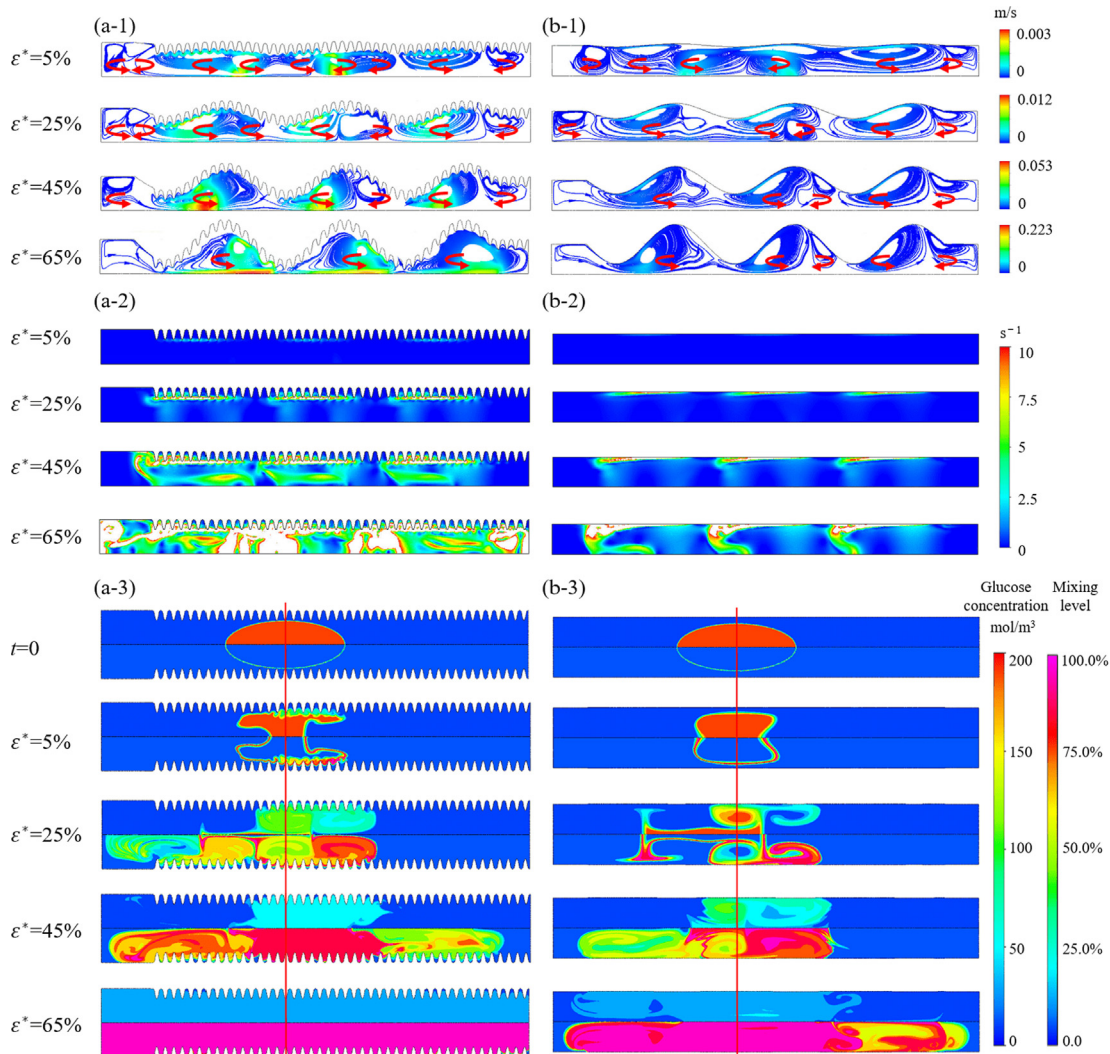


**Fig. 10.** Comparison between cases with different  $\epsilon^*$  but the same  $f$  (i.e., 10 cycles/min, Set 3 in Table 2): (a) System 1; and (b) System 2. (a-1) and (b-1) display velocity streamlines at  $T/4$ ; (a-2) and (b-2) show strain rates at  $T/2$ , strain rate values higher than  $10 \text{ s}^{-1}$  are not plotted; (a-3) and (b-3) are concentration and mixing level hybrid plots at 0 s and 60 s (i.e.,  $10T$ ). Thick red and blue arrows have been added to show the flow direction. Solid red lines indicate the initial central position of the glucose block.

amplitude ratio of 5%, mixing is quite limited. The glucose block only experiences a shape change with certain noticeable mixing level values on its boundary alone (see Fig. 10(a-3) at  $\epsilon^* = 5\%$ ). Increasing the amplitude ratio intensifies both radial and axial mixing. When the contraction amplitude reaches 65%, the high speed and high strain rates lead to an almost thorough mixing. The same trends can be observed for System 2. Comparisons between subplots in Fig. 10(a) and (b) illustrate the mixing intensification effect of circular folds. This intensification effect increases for higher amplitude ratios.

Simulations in Set 6 compare cases under different frequencies but the same amplitude ratio, i.e., 25%. Velocity streamlines, shear rate distributions and the corresponding 2D hybrid plots are given in Fig. 11.

For System 1, the vortices under different frequencies lead to almost the same pattern, whereas the velocity magnitude increases with the frequency (Fig. 11(a-1)). The same amplitude and wavelength result in very similar vortex patterns. The increase in frequency indicates a shorter contraction cycle, leading to an increase in fluid velocity. The shear rate has a distribution similar to that of the base case, and its intensity slightly increases with the increase in frequency (Fig. 11(a-2)). As a result, both radial

and axial mixing can be enhanced by increasing the frequency (Fig. 11(a-3)). It should also be noted that within a specified total time of the mixing process (i.e., 60 s), a higher frequency means more cycles of segmentation movement, which contributes positively to mixing as well. The same trends can be observed for System 2. However, once again, circular folds offer better mixing performance ((a-3) vs. (b-3) in Fig. 11).

The final states in Fig. 11(a-3) and (b-3) are far from a thorough mixing. It can be assumed that further increases in frequency would lead to better mixing performance. However, the frequency of 12 cycles/min is already a very high value, which occurs only under extreme conditions (Hall, 2016). Considering physiological limitations, amplitude has a greater influence on both radial and axial mixing compared to frequency (see comparison between Figs. 11 and 10).

In addition to the simulations in Set 3 and Set 6 discussed above, six other sets were considered for a comprehensive study (Table 2). Fig. 12(a) and (b) summarize and compare mixing performance under a variety of amplitudes and frequency conditions for systems with and without circular folds. Most  $Re$  and  $Pe$  curves exhibit a "W" shape like the ones in the base case, except for the cases with the maximum amplitude ratio (i.e., 65%) for System 1.

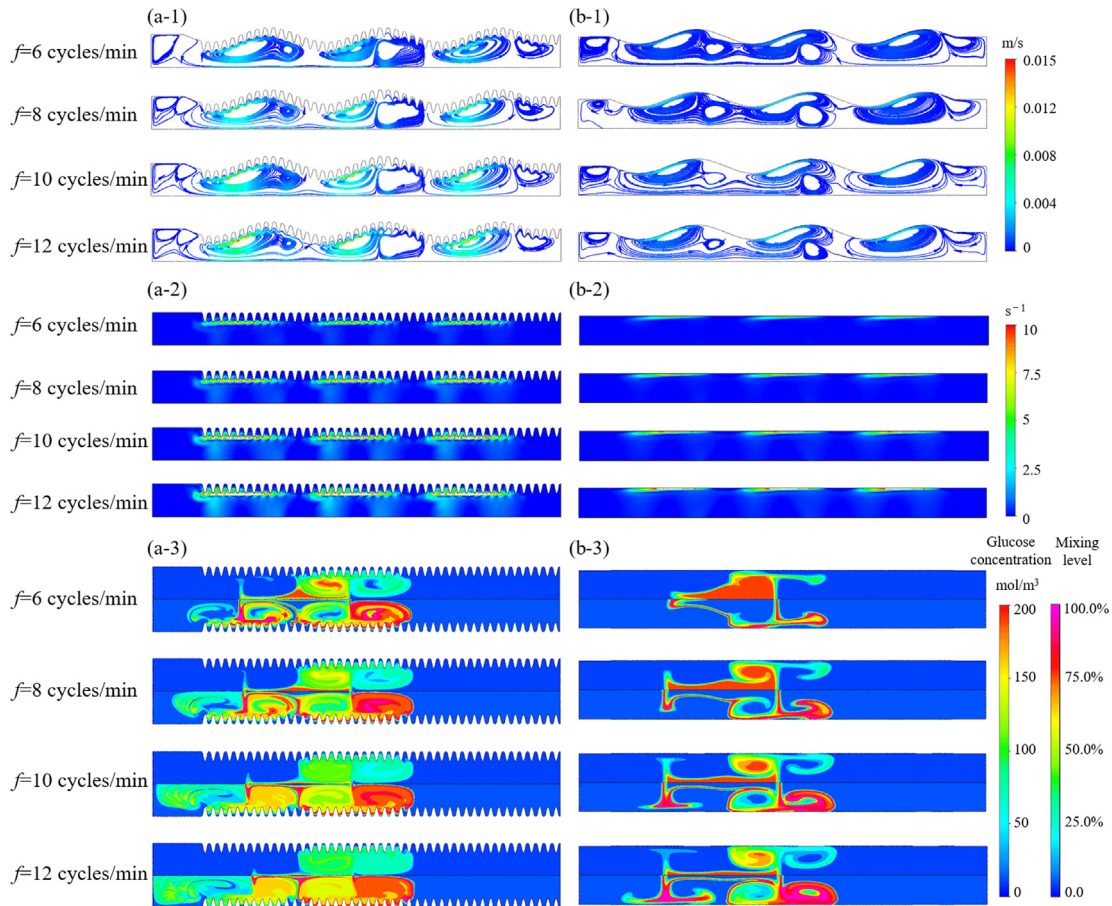


**Fig. 11.** Comparison between cases with different  $f$  but the same  $\varepsilon^*$  (i.e., 25%, Set 6 in Table 2): (a) System 1; and (b) System 2. (a-1) and (b-1) display velocity streamlines at  $T/4$ ; (a-2) and (b-2) show strain rates at  $T/2$ , strain rate values higher than  $10 \text{ s}^{-1}$  are not plotted; (a-3) and (b-3) are concentration and mixing level hybrid plots at 60 s.

This is because in System 1, the contraction amplitude ratio of 65% makes the lumen very narrow near the contraction positions of the intestinal lumen, thus producing a very high velocity at  $T/4$  and  $3T/4$  (see Fig. 10(a-1)). Fig. 12(a) also shows that increasing either amplitude or frequency can lead to an increase in  $Re$  and  $Pe$  and, hence, an increase in the mixing level (Fig. 12(b)). These findings can be qualitatively validated by the experimental results in Xiao et al. (2018) and Delaplace et al. (2018), where the effects of frequency and maximum penetration depth of the beater on mixing in a soft elastic reactor (SER) have been analyzed. The same trend was reported.

Moreover, even with the largest amplitude ratio of 65% and the largest frequency of 12 cycles/min, the flow is still laminar in the intestinal lumen (see the  $Re$  values in Fig. 12(a)). For System 1,  $Pe$  is 6079 at  $f = 6$  cycles/min and  $\varepsilon^* = 5\%$ . For System 2,  $Pe$  is 4277 at  $f = 6$  cycles/min and  $\varepsilon^* = 5\%$ . The value is always much larger than 1, even for the case with the minimum amplitude and frequency, indicating that the dominant mixing mechanism is convection caused by wall movement rather than molecular diffusion. Fig. 12(b) also shows that when the amplitude ratio is small (e.g., 5%), the mixing level is very low, implying a digestion problem. For elderly or sick people, low-amplitude segmentation motility may be a key factor for their digestion and may lead to absorption-related diseases.

When comparing the two systems, it was observed that the  $Re$  and  $Pe$  values of System 1 are always greater than those of System 2 under the same amplitude and frequency. The enhancement ratio values are greater than 1. At the same frequency, the maximum enhancement ratio increases with the increase in amplitude. At

$f = 6$  cycles/min and  $\varepsilon^* = 65\%$ , the maximum enhancement ratio reached 6.18. These data clearly show the mixing intensification effect provided by the circular folds. Without circular folds, higher segmentation frequencies or amplitudes are needed to reach the same mixing level, which requires more energy and is sometimes not possible for the human digestive system.

The final mixing levels under different frequencies and amplitudes at the end of the mixing process (i.e., 60 s) for both systems are given in Fig. 13 as a surface plot. As expected, the surface of System 1 is always greater than the surface of System 2. This 3D surface plot can greatly facilitate mixing level prediction under any combination of segmentation amplitude ratios and frequencies as long as the values are within the investigated ranges.

### 3.3. Effects of different segmentation wavelengths on mixing

It is known that the contraction wave has a length of 7–10 cm for each segment (Wright et al., 2016). Wavelength values of 3, 5, 7 and 9 cm were selected for further study (i.e., Set 9 in Table 2). The velocity streamlines and the corresponding strain rates and 2D hybrid plots are given in Fig. 14.

Fig. 14 shows that increasing the wavelength leads to the reduction of the number of vortices and the high/low shear rate zones, whereas each of them takes up more space. At the same time, the velocity magnitude and intensity of strain rates in the lumen are enhanced when the wavelength is increased. It can be seen in Fig. 14(a-3) and (b-3) that mixing is restricted to local areas by small vortices when the wavelength is small. Axial mixing can be significantly improved by enlarging the wavelength.

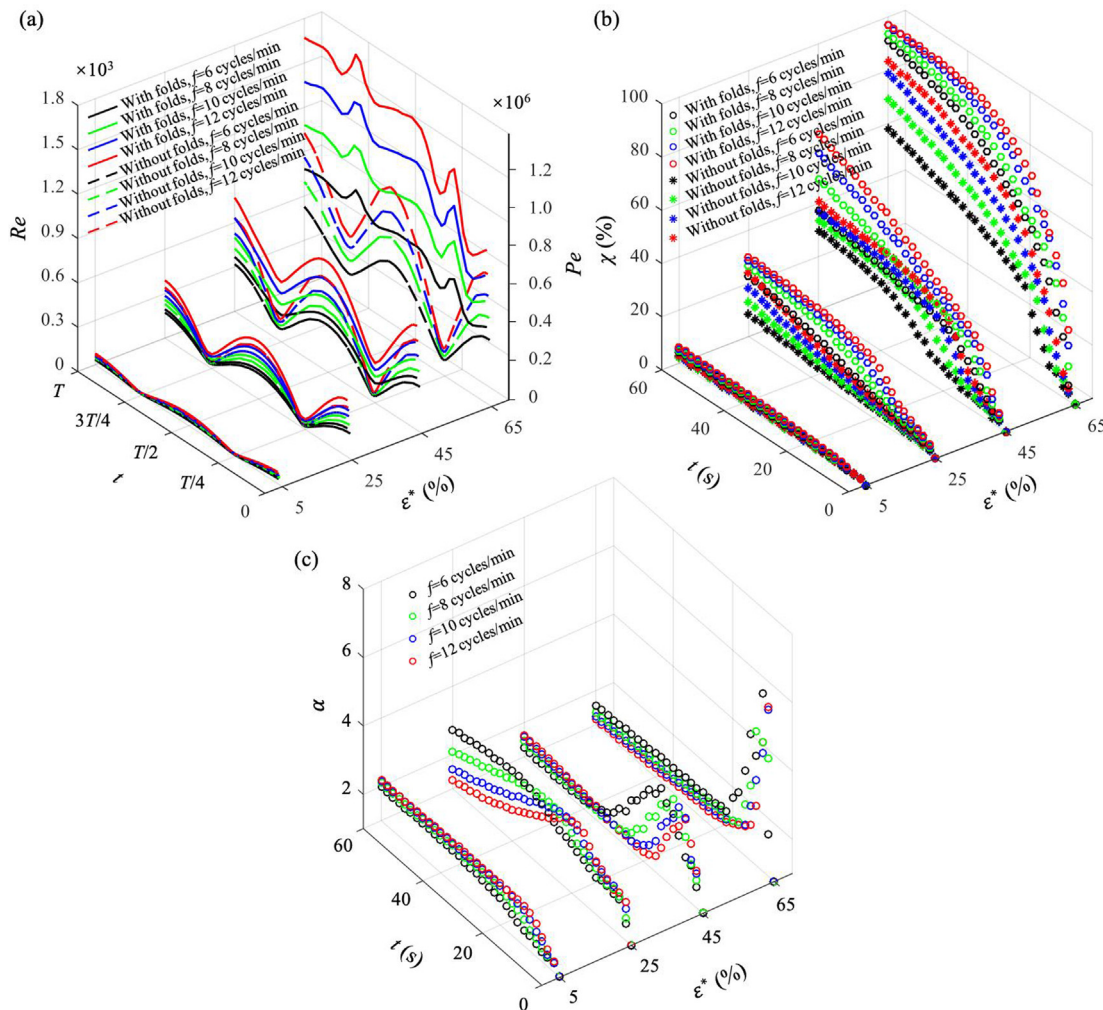


**Fig. 12.** The effect of segmentation amplitude and frequency on the evolution of: (a)  $Re$  and  $Pe$  over time in one cycle; (b) the mixing level in 60 s for both systems; and (c) the enhancement ratio in 60 s.

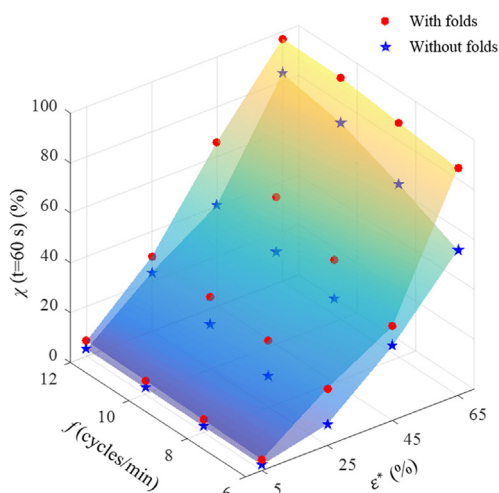


**Fig. 13.** Comparison of the final mixing level at 60 s under different  $f$  and  $\epsilon^*$  for both systems.

Consistent with the trends in velocity and shear rates, the  $Re$  and  $Pe$  values gradually increase as the wavelength increases (see Fig. 15(a)), resulting in a higher mixing level (see Fig. 15(b)). How-

ever, the maximum enhancement ratio decreases as the wavelength increases (see Fig. 15(c)). System 1 always performs better than System 2 in terms of mixing, regardless of the wavelength numbers selected in this study.

#### 3.4. Investigation of fold geometry

The results presented so far compare systems with and without circular folds. Detailed analyses demonstrate that the existence of folds is critical for adequate mixing and, hence, effective digestion. Fold geometry varies among individuals. In this section, different fold geometries are further investigated. The width of a fold is about 2–4 mm, whereas a fold wider than 5 mm is considered to be unusual (Krag, 1966). Since the presence of folds causes the intestinal surface area to increase by a factor of 1.57 to 3, the height of a fold is about 3 to 6 mm (Helander and Fandriks, 2014). In this study, the width of a fold,  $w_f$ , is 2, 3 or 4 mm, and the height,  $h_f$ , is 3, 4 or 5 mm (i.e., Set 10 in Table 2).

It can be seen from Fig. 16 that velocity streamlines and shear rates for systems with different folds are very similar, although not exactly the same. Increasing height-to-width ratio (i.e.,  $\xi$ ) leads to slight increases in both fluid velocity and the intensity of shear rates. This may be because the presence of folds with a larger height-to-width ratio reduces the free-flowing space in the intestinal cavity. Higher velocity and shear rates contribute to a more

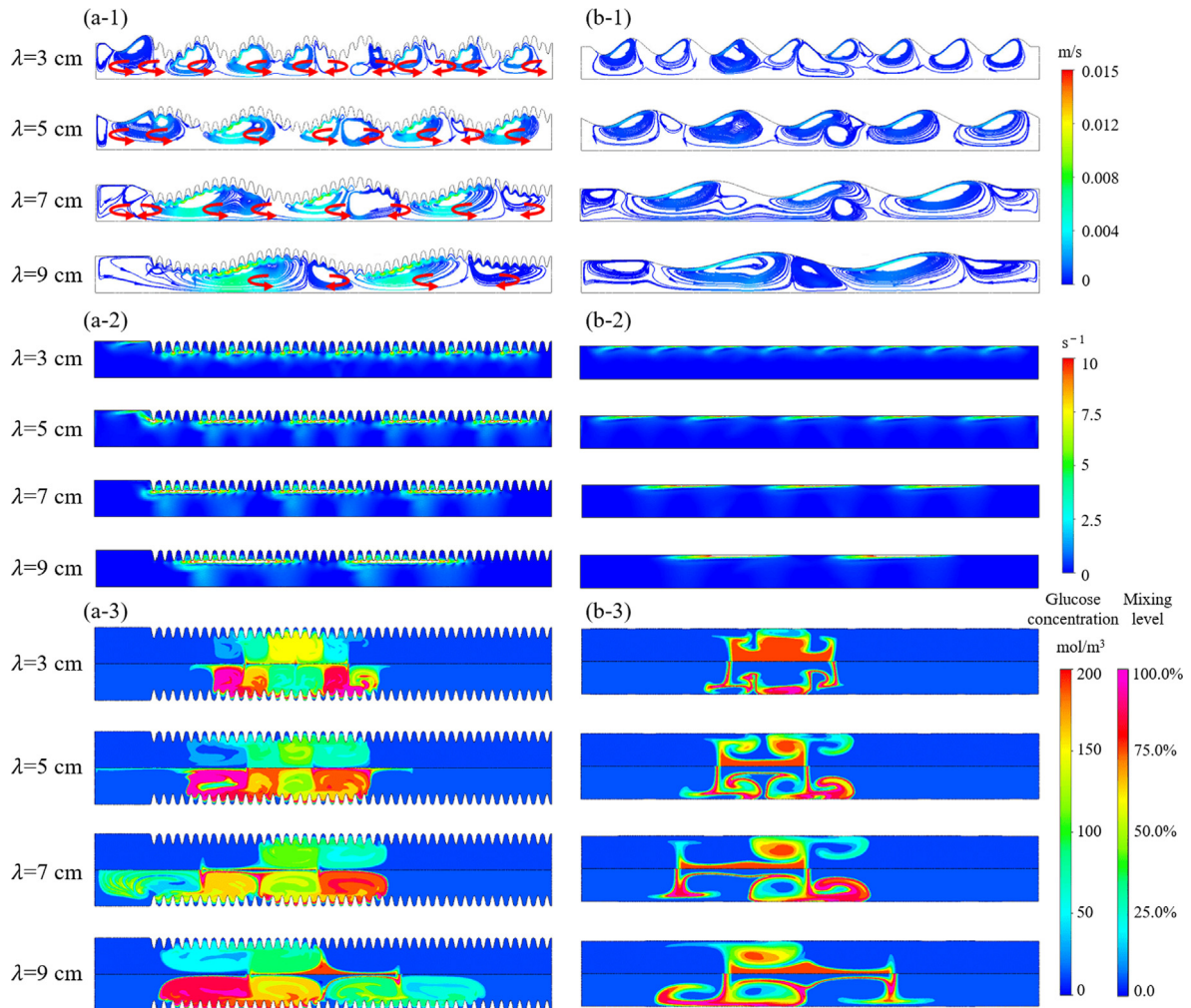


**Fig. 14.** Comparison between cases with different  $\lambda$  (i.e., Set 9 in Table 2): (a) System 1; and (b) System 2. (a-1) and (b-1) display velocity streamlines at  $T/4$ ; (a-2) and (b-2) show strain rates at  $T/2$ , strain rate values higher than  $10 \text{ s}^{-1}$  are not plotted; (a-3) and (b-3) are concentration and mixing level hybrid plots at 60 s. Thick red arrows have been added to show the vortex flow direction.

homogeneous concentration distribution (see Fig. 16(c)). At the same time, axial mixing is enhanced (see the mixing level distributions).

It can be observed in Fig. 17 that a larger value of  $\xi$  leads to higher  $Re$  and  $Pe$  values and, hence, a higher mixing level. The height-to-width ratio is thus a good variable to define fold geometry. These results imply that high and slim circular folds outperform short and fat ones in the mixing of chyme. A healthy fold is not wider than 5 mm and its height is greater than 3 mm and can even reach up to 8 mm in the jejunum. These features of the human intestine are conducive to adequate mixing performance.

#### 4. Conclusion

With the objective of understanding the function of the hierarchical structure of the inner intestinal surface in digestion and absorption, this study specifically investigated the circular folds on the inner surface of the duodenum and revealed quantitatively the influence of this particular structure on mixing intensification in the lumen. A specific 2D axisymmetric multiphysics model was developed that was able to simulate coupled momentum and mass transfer in a complex structured and dynamically evolving domain, i.e., a human duodenum with circular folds explicitly

modeled under segmentation contraction. In addition to tracking the flow and the nutrient concentration fields, it was possible to quantify a special mixing level field, together with the Reynolds number and the Peclet number. The methods implemented allowed us to understand the mixing process in a comprehensive and precise way.

Simulation results show that the circular folds can effectively intensify both radial and axial mixing under segmentation contraction. Compared to the system without circular folds, the system with folds demonstrates the following features: in the lumen, more prominent and long-lasting vortices can be identified; and higher fluid velocity and higher shear rates can be observed. These features lead to larger  $Re$  and  $Pe$  values and, hence, a higher mixing efficiency. For the duodenum with circular folds, mixing can be enhanced by increasing the frequency and/or amplitude of the segmentation contraction. Modulating the amplitude is found to be more effective. An enhancement ratio is defined to quantify the enhancement of mixing due to the introduction of the circular folds. This ratio evolves over time and demonstrates a maximum value. At the same frequency of the segmentation contraction, the maximum enhancement ratio increases with the increase in amplitude. At  $f = 6$  cycles/min and  $\varepsilon^* = 65\%$ , the maximum enhancement ratio can reach 6.18. A thorough mixing with a mixing level of 97.27% can be achieved at 60 s under  $f = 12$  cycles/min

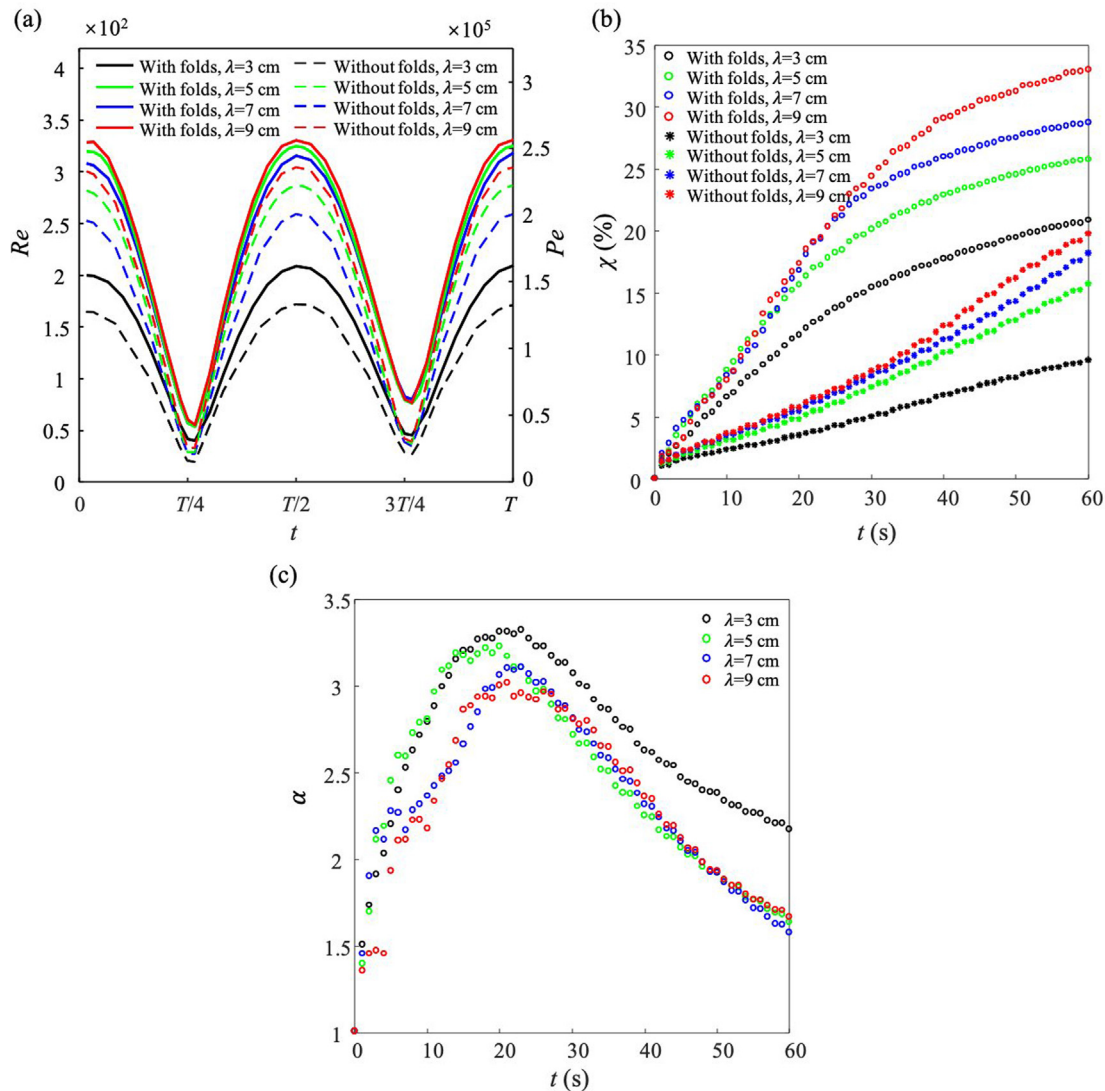


**Fig. 15.** The influence of the segmentation wavelength on the evolution of: (a)  $Re$  and  $Pe$  in one movement cycle; (b) the evolution of the mixing level for both systems; (c) the evolution of the enhancement ratio.

and  $\varepsilon^* = 65\%$ . While under the same conditions, the system without circular folds can only offer a mixing level of 83.22%. The wavelength of the segmentation should be not too small so that sufficient axial mixing can be achieved. Moreover, tall and slim circular folds outperform their short and fat counterparts in promoting mixing in the lumen.

The findings in the current study offer new insights into the function of the inner surface structure of the duodenum in terms of digestion and absorption. They will hopefully be able help doctors to understand and diagnose related diseases. Moreover, the structural effect of circular folds can inspire the optimized design of soft-elastic reactors that currently have smooth walls, and it is assumed that their mixing performance will be improved for practical applications (Delaplace et al., 2018, 2020; Li et al., 2019; Xiao et al., 2018; Zhang et al., 2019; Zou et al., 2020). Deshpande et al. (2020) designed a miniature air suction system for chemical sensors that could be used to detect toxic chemical gases. It will be interesting to investigate whether implementing a soft elastic wall for the air suction duct can improve the detection efficiency or not.

The multiscale structure of the inner intestinal wall with circular folds, villi and even microvilli should be addressed in future studies. In addition to mixing, absorption should also be taken into

account. Furthermore, various enzymatic reactions will be modeled for a more comprehensive simulation of the digestive process.

## Author contributions

Prof. Jie Xiao conceptualized the project, supervised the first and second authors, designed the simulation cases, developed analysis methods, analyzed the data and revised the manuscript. Ms. Jinping Zha carried out all simulations, analyzed the data and drafted the manuscript. Mr. Siyu Zou contributed to model development. Dr. Guillaume Delaplace and Prof. Romain Jeantet analyzed the results and revised the manuscript. Prof. Xiao Dong Chen, Dr. Didier Dupont, Prof. Jianyu Hao, Dr. Xinjuan Liu and Dr. Peng Wu were all involved in data analyses and discussions.

## Declaration of Competing Interest

The authors declare that they have no known competing financial interests or personal relationships that could have appeared to influence the work reported in this paper.

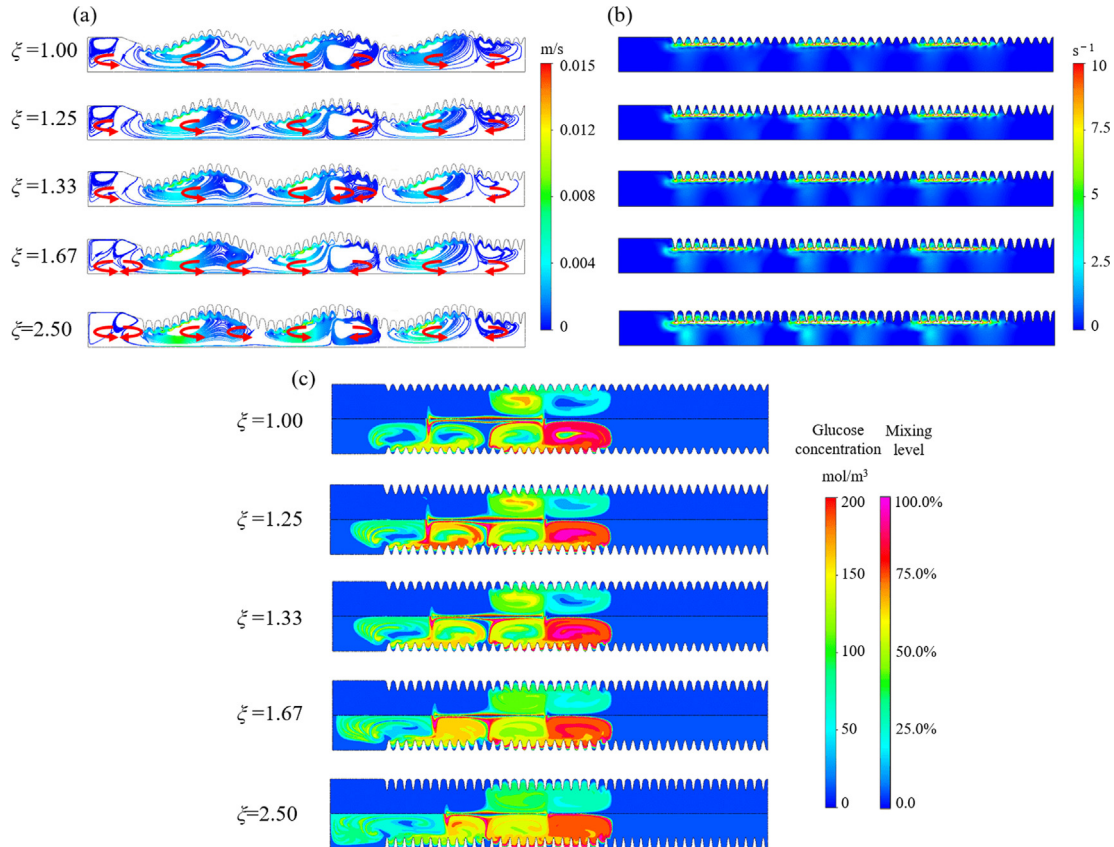


**Fig. 16.** Comparison between cases with different sizes of folds (i.e., Set 10 in Table 2): (a) velocity streamlines at  $T/4$ ; (b) strain rates at  $T/2$ , strain rate values higher than  $10 \text{ s}^{-1}$  are not plotted; and (c) concentration and mixing level hybrid plots at 60 s. Different height-to-width ratios were used:  $\xi = 1.00$ :  $h_f = 3 \text{ mm}$ ,  $w_f = 3 \text{ mm}$ ;  $\xi = 1.25$ :  $h_f = 5 \text{ mm}$ ,  $w_f = 4 \text{ mm}$ ;  $\xi = 1.33$ :  $h_f = 4 \text{ mm}$ ,  $w_f = 3 \text{ mm}$ ;  $\xi = 1.67$ :  $h_f = 5 \text{ mm}$ ,  $w_f = 3 \text{ mm}$ ;  $\xi = 2.50$ :  $h_f = 5 \text{ mm}$ ,  $w_f = 2 \text{ mm}$ .

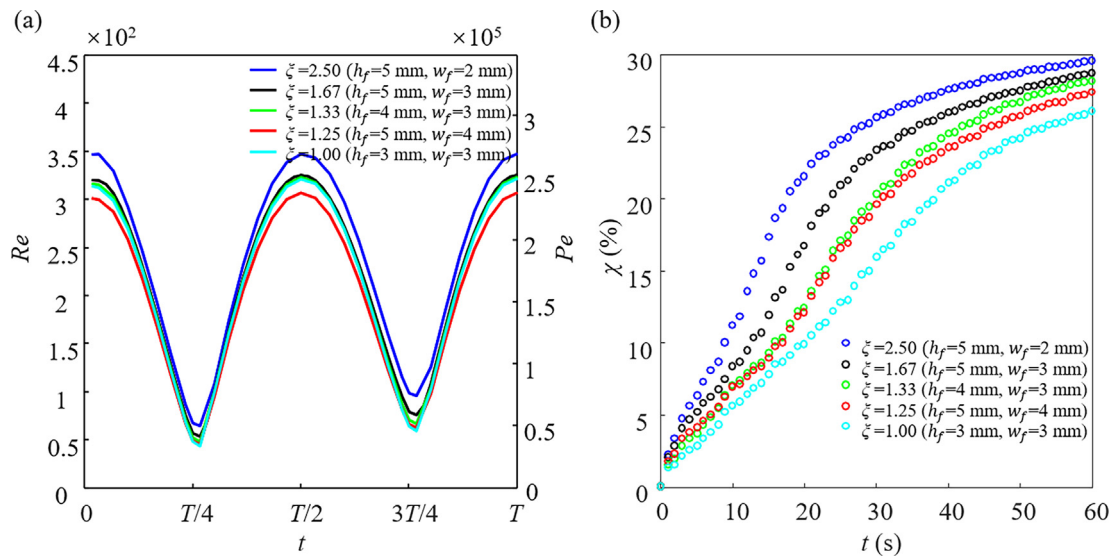


**Fig. 17.** The influence of fold geometry on the evolution of: (a)  $Re$  and  $Pe$  in one movement cycle; and (b) the mixing level in 60 s.

## Acknowledgements

The authors are grateful for the research funds provided by the National Natural Science Foundation of China (No. 21978184) and the Natural Science Foundation of Jiangsu Province (Grant No.

BK20170062). Supports from the National Key Research and Development Program of China (2016YFE0101200), the International Associated Laboratory – FOODPRINT (Soochow University (China) – INRAE and Institut Agro (France)), the “Jiangsu Specially-Appointed Professors Program”, “Jiangsu Innovation and

Entrepreneurship (Shuang Chuang) Program", and "Priority Academic Program Development (PAPD) of Jiangsu Higher Education Institutions" are also appreciated.

## Appendix A

The geometric details of the circular folds and the related calculations are given in this appendix. The folds are plotted as truncated sinusoidal waves connected by truncated circles. Mathematically, the section of the wave on the right side can be written as:

$$r = -h_f \cdot \sin\left(\frac{\pi}{w_f}(z - z_0)\right) \quad (\text{A1})$$

In order to obtain a smooth connection between the fold and the truncated circle, two shapes must share the same tangent line (i.e., the red line in Fig. A1), and the intersection point is  $(z_0, 0)$ .

The slope of the line at point  $(z_0, 0)$  (i.e., the derivative of the fold function with respect to  $z$  at  $(z_0, 0)$ ) can be expressed as:

$$r' = -h_f \cdot \frac{\pi}{w_f} \cdot \cos\left(\frac{\pi}{w_f}(z - z_0)\right) \quad (\text{A2})$$

$$r'|_{z=z_0} = -h_f \cdot \frac{\pi}{w_f} \quad (\text{A3})$$

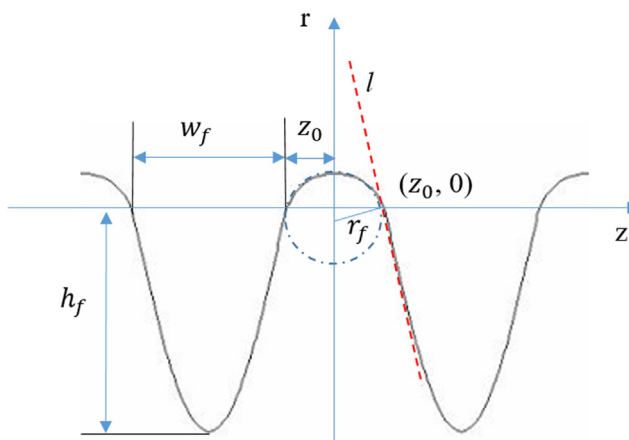


**Fig. A1.** Representation of two folds connected by a truncated circle: geometrical parameters.

Thus, the equation of the tangent line is:

$$h_f \cdot \frac{\pi}{w_f} \cdot z + r - h_f \cdot \frac{\pi}{w_f} \cdot z_0 = 0 \quad (\text{A4})$$

The distance from the center of the circle (i.e.,  $(0, -\sqrt{r_f^2 - z_0^2})$ ) to this tangent line is equal to the radius of the circle, which yields:

$$\frac{|0 + (-\sqrt{r_f^2 - z_0^2}) + (-h_f \cdot \frac{\pi}{w_f} \cdot z_0)|}{\sqrt{(h_f \cdot \frac{\pi}{w_f})^2 + 1}} = r_f \quad (\text{A5})$$

The radius of the circle can then be calculated as:

$$r_f = \frac{z_0 \cdot w_f}{\pi h_f} \sqrt{\left(\frac{\pi h_f}{w_f}\right)^2 + 1} \quad (\text{A6})$$

## Appendix B

**Fig. B1** gives a cross-sectional view of the circular folds. The equation of position deviation from a smooth tube due to the folds is derived in this appendix. The  $z$  axis is shifted upwards by  $R_0$  in order to facilitate the derivation of position deviation.

Three types of lines can be identified in **Fig. B1**, i.e., straight lines, folds and truncated circles. Thus piece-wise functions can be used to represent them.

When  $0 \leq z \leq a$ , it is a straight line, whose deviation from the smooth tube surface is 0:

$$F(z) = 0 \quad (\text{B1})$$

When  $a < z \leq a + z_0$ , the equation for the arc segment can be written as:

$$(z - a)^2 + (r + r_f)^2 = r_f^2 \quad (\text{B2})$$

Rearranging this equation to yield  $r$ :

$$r = \pm \sqrt{r_f^2 - (z - a)^2} - r_f \quad (\text{B3})$$

Since the arc is one part of the upper half of the circle,  $r$  is then:

$$r = \sqrt{r_f^2 - (z - a)^2} - r_f \quad (\text{B4})$$

Thus, when  $a < z \leq a + z_0$ , the position deviation can be calculated as:

$$F(z) = \sqrt{r_f^2 - (z - a)^2} - r_f \quad (\text{B5})$$

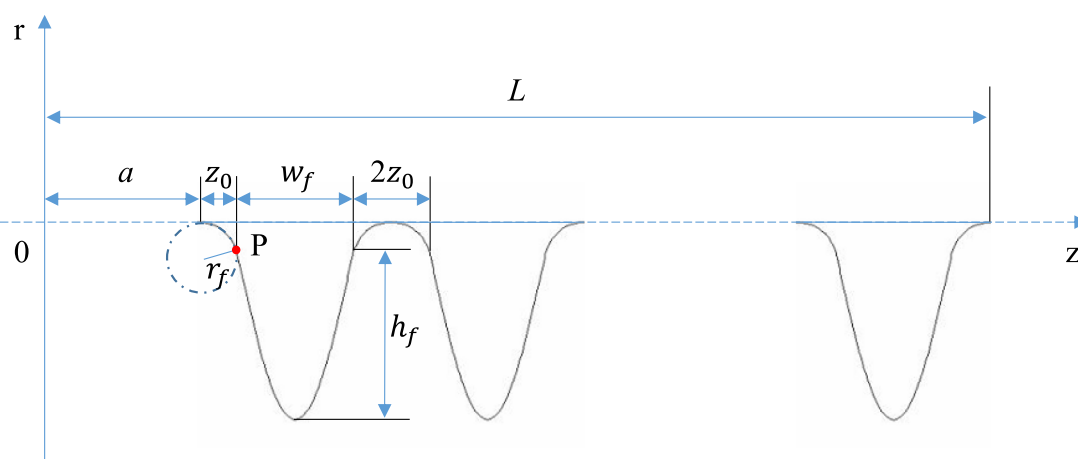


**Fig. B1.** Cross-sectional view of the circular folds' geometry.

The arc intersects with the fold at the position  $(a + z_0, \sqrt{r_f^2 - z_0^2} - r_f)$ . When  $a + z_0 < z \leq a + z_0 + w_f$ , the equation of the fold becomes:

$$F(z) = (\sqrt{r_f^2 - z_0^2} - r_f) - h_f \cdot \sin\left(\frac{\pi}{w_f}(z - (a + z_0))\right) \quad (B6)$$

Integrating Eqs. (B1), (B5) and (B6) offers the function of the first section of the curve, which includes the first fold (i.e.,  $n = 1$ ):

$$F(z) = \begin{cases} 0, & \text{when } z \in [0, a] \\ \sqrt{r_f^2 - (z - a)^2} - r_f, & \text{when } z \in (a, a + z_0] \\ (\sqrt{r_f^2 - z_0^2} - r_f) - h_f \cdot \sin\left(\frac{\pi}{w_f}(z - (a + z_0))\right), & \text{when } z \in (a + z_0, a + z_0 + w_f] \end{cases} \quad (B7)$$

The function for the complete curve becomes:

$$F(z) = \begin{cases} 0, & \text{when } z \in [0, a] \\ \sqrt{r_f^2 - (z - (a + 2(n-1)z_0 + (n-1)w_f))^2} - r_f, & \text{when } z \in (a + (2n-3)z_0 + (n-1)w_f, a + (2n-1)z_0 + (n-1)w_f] \cap (a, L] \\ (\sqrt{r_f^2 - z_0^2} - r_f) - h_f \cdot \sin\left(\frac{\pi}{w_f}(z - (a + (2n-1)z_0 + (n-1)w_f))\right), & \text{when } z \in (a + (2n-1)z_0 + (n-1)w_f, a + (2n-1)z_0 + w_f] \cap (a, L] \end{cases} \quad (B8)$$

where  $n$  is the index of the circular folds.

## References

- Barrett, K.E., Barman, S.M., Boitano, S., Brooks, H.L., 2016. Ganong's Review of Medical Physiology. McGraw-Hill Education, New York.
- Bayliss, W.M., Starling, E.H., 1899. The movements and innervation of the small intestine. *J. Physiol.* 24, 99–143.
- Bornhorst, G.M., Chang, L.Q., Rutherford, S.M., Moughan, P.J., Singh, R.P., 2013. Gastric emptying rate and chyme characteristics for cooked brown and white rice meals in vivo. *J. Sci. Food Agric.* 93, 2900–2908.
- Cannon, W.B., 1902. The movements of the intestines studied means of the roentgen rays. *Am. J. Physiol.* 6, 251–277.
- Chen, L., Xu, Y., Fan, T., Liao, Z., Wu, P., Wu, X., Chen, X.D., 2016. Gastric emptying and morphology of a 'near real' in vitro human stomach model (RD-IV-HSM). *J. Food Eng.* 183, 1–8.
- de Loubens, C., Lente, R.G., Hulls, C., Janssen, P.W.M., Love, R.J., 2014. Characterisation of mixing in the proximal duodenum of the rat during longitudinal contractions and comparison with a fluid mechanical model based on spatiotemporal motility data. *PLoS ONE* 9, e95000.
- de Loubens, C., Lente, R.G., Love, R.J., Hulls, C., Janssen, P.W.M., 2013. Fluid mechanical consequences of pendular activity, segmentation and pyloric outflow in the proximal duodenum of the rat and the guinea pig. *J. R. Soc. Interface* 10, 20130027.
- Delaplace, G., Gu, Y., Liu, M., Jeantet, R., Xiao, J., Chen, X.D., 2018. Homogenization of liquids inside a new soft elastic reactor: Revealing mixing behavior through dimensional analysis. *Chem. Eng. Sci.* 192, 1071–1080.
- Delaplace, G., Liu, M.H., Jeantet, R., Xiao, J., Chen, X.D., 2020. Predicting the mixing time of soft elastic reactors: Physical models and empirical correlations. *Ind. Eng. Chem. Res.* 59, 6258–6268.
- Deng, R., Pang, L., Xu, Y., Li, L., Wu, X., Chen, X.D., 2014. Investigation on a soft tubular model reactor based on bionics of small intestine – residence time distribution. *Int. J. Food Eng.* 10, 645–655.
- Deshpande, M.D., Sivapragasam, M., Umesh, S., 2020. An efficient miniature air suction system for chemical sensors for micro air vehicle application. *Sadhana-Acad. Proc. Eng. Sci.* 45, 116.
- Fullard, L., Lammer, W., Wake, G.C., Ferrua, M.J., 2014. Propagating longitudinal contractions in the ileum of the rabbit - efficiency of advective mixing. *Food Funct.* 5, 2731–2742.
- Fullard, L.A., Lammer, W.J., Ferrua, M.J., 2015. Advective mixing due to longitudinal and segmental contractions in the ileum of the rabbit. *J. Food Eng.* 160, 1–10.
- Gousseti, O., Jaime-Fonseca, M.R., Fryer, P.J., Mills, C., Wickham, M.S.J., Bakalis, S., 2014. Hydrocolloids in human digestion: Dynamic in-vitro assessment of the effect of food formulation on mass transfer. *Food Hydrocolloids* 42, 378–385.
- Gousseti, O., Lovegrove, A., Kosik, O., Fryer, P.J., Mills, C., Gates, F., Tucker, G., Latty, C., Shewry, P., Bakalis, S., 2019. Exploring the role of cereal dietary fiber in digestion. *J. Agric. Food. Chem.* 67, 8419–8424.
- Hall, J.E., 2016. Guyton and Hall Textbook of Medical Physiology. Elsevier Saunders, The United States of America.
- Helander, H.F., Fandriks, L., 2014. Surface area of the digestive tract-revisited. *Scand. J. Gastroenterol.* 49, 681–689.
- Hua, X.L., Zhang, Y.N., Dong, Z.Z., Wang, Y., Chen, X.D., Xiao, J., 2020. Simulation and analysis of mass transfer and absorption process intensification by villi movement. *Off. J. Chem. Ind. Eng. Soc. China (CIESC J.)* 71, 2024–2034.
- Husebye, E., 1999. The patterns of small bowel motility: physiology and implications in organic disease and functional disorders. *Neurogastroenterol. Motil.* 11, 141–161.
- Ishikawa, T., Sato, T., Mohit, G., Imai, Y., Yamaguchi, T., 2011. Transport phenomena of microbial flora in the small intestine with peristalsis. *J. Theor. Biol.* 279, 63–73.
- Krag, E., 1966. Enlarged gastric and duodenal rugae. *Acta Medica Scandinavica* 179, 343–348.
- Leiper, J.B., 2015. Fate of ingested fluids: factors affecting gastric emptying and intestinal absorption of beverages in humans. *Nutr. Rev.* 73, 57–72.
- Lente, R.G., de Loubens, C., 2015. A review of mixing and propulsion of chyme in the small intestine: fresh insights from new methods. *J. Comparat. Physiol. B-Biochem. Syst. Environ. Physiol.* 185, 369–387.
- Lente, R.G., Janssen, P.W.M., 2011. The Physical Processes of Digestion. Springer, New York.
- Lente, R.G., Janssen, P.W.M., Deloubens, C., Lim, Y.F., Hulls, C., Chambers, P., 2013. Mucosal microfolds augment mixing at the wall of the distal ileum of the brushtail possum. *Neurogastroenterol. Motil.* 25, 881–e700.
- Li, C., Xiao, J., Zhang, Y., Chen, X.D., 2019. Mixing in a Soft-Elastic Reactor (SER): A simulation study. *Can. J. Chem. Eng.* 97, 676–686.
- Lim, Y.F., de Loubens, C., Love, R.J., Lente, R.G., Janssen, P.W., 2015. Flow and mixing by small intestine villi. *Food Funct.* 6, 1787–1795.
- Liu, M., Xiao, J., Chen, X.D., 2018a. A Soft-Elastic Reactor (SER) inspired from animal upper digestion tract. *Chem. Eng. Technol.* 41, 1051–1056.
- Liu, M., Zou, C., Xiao, J., Chen, X.D., 2018b. Soft-elastic bionic reactor. *Off. J. Chem. Ind. Eng. Soc. China (CIESC J.)* 69, 414–422.
- Macagno, E.O., Christensen, J., 1980. Fluid mechanics of the duodenum. *Annu. Rev. Fluid Mech.* 12, 139–158.
- Marieb, E.N., Keller, S.M., 2018. Essentials of Human Anatomy & Physiology. Pearson Education, London.
- Martini, F.H., Nath, J.L., Bartholomew, E.F., 2012. Fundamentals of Anatomy & Physiology. Pearson Education, San Francisco.
- Sarna, S., Condon, R.E., Cowles, V., 1983. Enteric mechanisms of initiation of migrating myoelectric complexes in dogs. *Gastroenterology* 84, 814–822.
- Sherwood, L., 2011. Fundamentals of Human Physiology. Cengage Learning, Canada.
- Sinnott, M.D., Cleary, P.W., Arkwright, J.W., Dinning, P.G., 2012. Investigating the relationships between peristaltic contraction and fluid transport in the human colon using Smoothed Particle Hydrodynamics. *Comput. Biol. Med.* 42, 492–503.
- Sinnott, M.D., Cleary, P.W., Harrison, S.M., 2017. Peristaltic transport of a particulate suspension in the small intestine. *Appl. Math. Model.* 44, 143–159.
- Standring, S., 2008. Gray's Anatomy: The Anatomical Basis of Clinical Practice. Elsevier Churchill Livingstone, London.
- Takahashi, T., 2011. Flow Behavior of digesta and the absorption of nutrients in the gastrointestinal. *J. Nutr. Sci. Vitaminol.* 57, 265–273.
- Wright, N.D., Kong, F., Williams, B.S., Fortner, L., 2016. A human duodenum model (HDM) to study transport and digestion of intestinal contents. *J. Food Eng.* 171, 129–136.
- Wu, P., Bhattacharai, R.R., Dhital, S., Deng, R., Chen, X.D., Gidley, M.J., 2017a. In vitro digestion of pectin- and mango-enriched diets using a dynamic rat stomach-duodenum model. *J. Food Eng.* 202, 65–78.
- Wu, P., Deng, R., Wu, X., Wang, Y., Dong, Z., Dhital, S., Chen, X.D., 2017b. In vitro gastric digestion of cooked white and brown rice using a dynamic rat stomach model. *Food Chem.* 237, 1065–1072.
- Xiao, J., Zou, C., Liu, M., Zhang, G., Delaplace, G., Jeantet, R., Chen, X.D., 2018. Mixing in a soft-elastic reactor (SER) characterized using an RGB based image analysis method. *Chem. Eng. Sci.* 181, 272–285.
- Zhang, G.D., Liu, M.H., Zou, C., Xiao, J., Chen, X.D., 2019. Enhancement of liquid mixing in a soft-elastic reactor based on bionics with an elastic rod. *Chem. Ind. Eng. Progr.* 38, 826–833.
- Zhang, X., Liao, Z., Wu, P., Chen, L., Chen, X.D., 2018. Effects of the gastric juice injection pattern and contraction frequency on the digestibility of casein powder suspensions in an in vitro dynamic rat stomach made with a 3D printed model. *Food Res. Int.* 106, 495–502.
- Zhang, Y., Wu, P., Jeantet, R., Dupont, D., Delaplace, G., Chen, X.D., Xiao, J., 2020. How motility can enhance mass transfer and absorption in the duodenum: Taking the structure of the villi into account. *Chem. Eng. Sci.* 213, 115406.
- Zou, J., Xiao, J., Zhang, Y., Li, C., Chen, X.D., 2020. Numerical simulation of the mixing process in a soft elastic reactor with bionic contractions. *Chem. Eng. Sci.* 220, 115623.
- Zuo, J.Y., Gisolf, A., Wang, K., Dubost, F., Pfeiffer, T., Dumont, H., Mishra, V., Chen, L., Agarwal, A., Ayan, C., Mullins, O.C., 2016. Quantitative mixing rules for downhole oil-based mud contamination monitoring in real time using multiple sensors. *J. Petrol. Sci. Eng.* 137, 214–226.